

A comparison of linear interpolation models for iterative CT reconstruction

Katharina Hahn^{a)}

Pattern Recognition Laboratory, Department of Computer Science, Friedrich–Alexander–Universität, Erlangen–Nürnberg, Martensstr. 3, 91058 Erlangen, Germany; Siemens Healthcare, GmbH 91301, Forchheim, Germany; and Department of Radiology, University of Utah, Salt Lake City, Utah 84108

Harald Schöndube and Karl Stierstorfer

Siemens Healthcare, GmbH 91301, Forchheim, Germany

Joachim Hornegger

Pattern Recognition Laboratory, Department of Computer Science, Friedrich–Alexander–Universität, Erlangen–Nürnberg, Martensstr. 3, 91058 Erlangen, Germany

Frédéric Noo^{b)}

Department of Radiology, University of Utah, Salt Lake City, Utah 84108

(Received 20 June 2016; revised 25 August 2016; accepted for publication 12 October 2016; published 11 November 2016)

Purpose: Recent reports indicate that model-based iterative reconstruction methods may improve image quality in computed tomography (CT). One difficulty with these methods is the number of options available to implement them, including the selection of the forward projection model and the penalty term. Currently, the literature is fairly scarce in terms of guidance regarding this selection step, whereas these options impact image quality. Here, the authors investigate the merits of three forward projection models that rely on linear interpolation: the distance-driven method, Joseph's method, and the bilinear method. The authors' selection is motivated by three factors: (1) in CT, linear interpolation is often seen as a suitable trade-off between discretization errors and computational cost, (2) the first two methods are popular with manufacturers, and (3) the third method enables assessing the importance of a key assumption in the other methods.

Methods: One approach to evaluate forward projection models is to inspect their effect on discretized images, as well as the effect of their transpose on data sets, but significance of such studies is unclear since the matrix and its transpose are always jointly used in iterative reconstruction. Another approach is to investigate the models in the context they are used, i.e., together with statistical weights and a penalty term. Unfortunately, this approach requires the selection of a preferred objective function and does not provide clear information on features that are intrinsic to the model. The authors adopted the following two-stage methodology. First, the authors analyze images that progressively include components of the singular value decomposition of the model in a reconstructed image without statistical weights and penalty term. Next, the authors examine the impact of weights and penalty on observed differences.

Results: Image quality metrics were investigated for 16 different fan-beam imaging scenarios that enabled probing various aspects of all models. The metrics include a surrogate for computational cost, as well as bias, noise, and an estimation task, all at matched resolution. The analysis revealed fundamental differences in terms of both bias and noise. Task-based assessment appears to be required to appreciate the differences in noise; the estimation task the authors selected showed that these differences balance out to yield similar performance. Some scenarios highlighted merits for the distance-driven method in terms of bias but with an increase in computational cost. Three combinations of statistical weights and penalty term showed that the observed differences remain the same, but strong edge-preserving penalty can dramatically reduce the magnitude of these differences.

Conclusions: In many scenarios, Joseph's method seems to offer an interesting compromise between cost and computational effort. The distance-driven method offers the possibility to reduce bias but with an increase in computational cost. The bilinear method indicated that a key assumption in the other two methods is highly robust. Last, strong edge-preserving penalty can act as a compensator for insufficiencies in the forward projection model, bringing all models to similar levels in the most challenging imaging scenarios. Also, the authors find that their evaluation methodology helps appreciating how model, statistical weights, and penalty term interplay together. © 2016 American Association of Physicists in Medicine. [<http://dx.doi.org/10.1118/1.4966134>]

Key words: iterative CT, image reconstruction, forward projection, image quality, distance-driven

1. INTRODUCTION

Nonlinear iterative reconstruction methods have become a topic of active research in x-ray computed tomography (CT). This effort is motivated by increasing evidence that such methods may enable improvements in image quality at equal dose or savings in radiation dose at equal image quality. See, e.g., the clinical studies in Refs. 1–7. Unlike classical filtered backprojection, iterative reconstruction methods allow including additional information in the reconstruction process, such as photon statistics for the measurements (Ref. 8, Chapter 2), physical properties of the x-ray beam,^{9–11} and image constraints.¹² These advantages all contribute to the observed improvements in the image quality.

Multidirectional investigations are required to gain the most out of nonlinear iterative reconstruction methods. One direction is the development of efficient algorithms for routine clinical CT scans. For this effort, the image is usually defined as the solution of a penalized weighted least-square model.^{13–16} Given that computer resources are naturally limited, the final image is always defined as the result of a finite number of iterations. However, the iterations may either be converging or semiconverging. Examples of popular optimization algorithms with converging iterations include the iterative coordinate descent (ICD) method^{12,17–21} and accelerated gradient-descent methods.^{22–25} Converging iterations are attractive in that they can provide solutions of arbitrary accuracy relative to the targeted image (i.e., the solution of the selected optimization problem), but many iterations may be needed, which complicates utilization when fast patient throughput is needed. Examples of algorithms with semiconverging iterations include IFBP,²⁶ ordered subsets methods,^{27–30} and accelerated versions of ordered subset methods.^{31–33} The hope with semiconverging iterations is to obtain, with a relatively small number of iterations and before divergence happens, a good approximation to the targeted image. Intrinsic to the development of all algorithms is the need for a fast implementation, using either CPU or GPU depending on the specifics of the algorithm.^{34–41}

Two other directions where progress is being made is reconstruction from limited data using total variation minimization and reconstruction from dual energy scans. Total variation has been shown to enable robust reconstructions from few projections (see, e.g., Ref. 42 and references therein), which, in CT, can be particularly useful for dynamic imaging.⁴³ Total variation has also been shown to be a useful constraint in interior tomography.^{44,45} Interesting contributions on iterative reconstruction in dual energy CT include those from Refs. 46–52.

Another important direction of research is the quantitative analysis of image quality dependence on numerous factors involved in the reconstruction process. Our contribution here belongs to this category. The literature on this direction of research is currently relatively scarce, so that our contribution helps filling an important gap in knowledge. Given that nonlinear iterative reconstruction methods come with an incredibly large number of degrees of freedom, the analysis is particularly challenging. The list of factors starts with the

selection of the objective function that defines the final image, then quickly expands to encompass a variety of parameters appearing in this function along with the forward projection model. Investigations in this direction are further complicated by the need to perform several reconstructions to account for different noise realizations and variations in geometry, which is essential for meaningful observations. One way to mitigate this difficulty is to focus on 2D rather than 3D reconstruction, with the hope that the acquired knowledge extends to 3D, at least partly.

In this paper, we investigate the impact of the forward projection model on image quality. Even though we only investigate this one factor, choices had to be made since the list of suggested forward projection models is fairly long; see, e.g., Refs. 53–65 for 2D and 3D examples. We decided to focus the study on the following three forward projection models in 2D fan-beam CT geometry: Joseph's method,⁵³ the distance-driven method,⁶⁰ and the bilinear method.⁶⁶ A first reason motivating this selection is the fact that all three methods are based on linear interpolation, which is typically seen as a suitable trade-off between discretization errors and computational effort for image reconstruction in diagnostic CT. Algorithms that rely on nearest neighbor interpolation, such as the popular method of Siddon,⁵⁴ tend to lack robustness for utilization in diagnostic CT, unless countermeasures are taken.⁶⁷ Second, all three methods are such that they can be easily extended to 3D CT geometries, as shown in Refs. 58, 64, and 68. Third, these methods are popular with manufacturers, particularly the first two, which seem to be used in clinical products. Fourth, knowledge on the behavior of these important methods is currently fairly limited for diagnostic CT geometries; see Refs. 64, 68, and 69. See also Ref. 70 for a complementary study on the effect of forward projection models for few view tomography with total variation regularization.

Investigating the impact of forward projection models on image quality is not straightforward. A critical question was to decide if the models should be investigated on their own or in the context of iterative CT reconstruction with a specific objective function that includes typical ingredients such as statistical weights and a penalty term. We selected the former option, as we felt that a primary goal should be to first understand what the model can offer on its own. The impact of statistical weights and penalty terms may then be easier to understand in a second stage of investigations. One approach to investigate the value of the models on their own would be to use the singular value decomposition. Such an approach would provide a complete picture in terms of recoverable features and associated stability, but this picture may be too rich to fully comprehend. We settled down for an intermediate approach that progressively injects components of the singular value decomposition in a reconstructed image and relies on classical image quality metrics.

The paper is organized as follows. First, the scanner geometry chosen for comparison is described in Sec. 2, along with a brief description of the three forward projection models, as well as a short discussion highlighting fundamental differences between them. Next, Sec. 3 explains the

experimental comparison conditions, including the image formation process, geometrical settings, and the phantom used for testing. This section is followed by Sec. 4, which gives a detailed description of basic and task-based metrics used for quantitative comparison, and by Sec. 5, which presents and discusses the results obtained with these metrics. Next, in Sec. 6, we examine examples of image reconstruction with statistical weights and penalty terms. Finally, a summary discussion and conclusions are given in Sec. 7.

2. BACKGROUND

We start with a description of the 2D fan-beam data acquisition geometry used for our investigation. Next, a brief review of the three linear interpolation models under comparison is given. This review is followed by a comparative discussion of key features of these models.

2.A. Fan-beam geometry

The geometry of a 3rd generation CT scanner with a curved detector is used for data simulation, as shown in Fig. 1. In this geometry, the x-ray source rotates synchronously with the detector around a fixed center, thereby generating fan-beam data.

Let λ be the polar angle measured relatively to the x -axis, and let $\underline{e}_u(\lambda) = [-\sin(\lambda), \cos(\lambda)]^T$ and $\underline{e}_w(\lambda) = [\cos(\lambda), \sin(\lambda)]^T$ be two orthogonal unit vectors, where the superscript T denotes the transpose operator. Then, the circular scanning path is defined as

$$\underline{a}(\lambda) = R_0 \underline{e}_w(\lambda) + \delta(\lambda) \underline{e}_u(\lambda) \quad \text{with} \quad \lambda \in [\lambda_s, \lambda_e], \quad (1)$$

where R_0 is the scan radius, i.e., the distance from the source to the rotation center, λ_s is the start angle, λ_e is the end angle, and $\delta(\lambda)$ accounts for a possible flying focal spot (FFS) feature during data acquisition.

When $\delta(\lambda) = 0$, the distance from the source, $\underline{a}(\lambda)$, to any point on the detector is D . Each point on the detector is

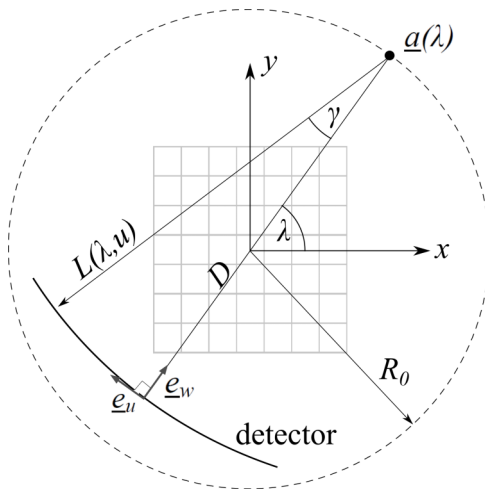


FIG. 1. Fan-beam geometry. Angle λ specifies the source position. The measurements at any given source position are identified using either γ or u , with $u = D\gamma$.

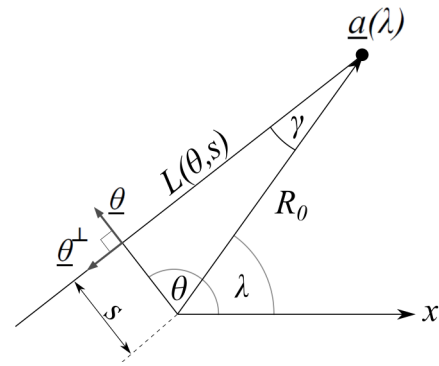


FIG. 2. Parallel-beam parametrization: line $L(\theta, s)$ represents the same measurement as $L(\lambda, \gamma)$ in Fig. 1.

identified using a curvilinear coordinate u that is positively measured on the detector in the direction of $\underline{e}_u(\lambda)$. The origin $u = 0$ coincides with the line that connects the source to the rotation center; this line is in the direction of $-\underline{e}_w(\lambda)$. Let $L(\lambda, u)$ be the ray that starts from $\underline{a}(\lambda)$ and goes toward the position u on the detector. The measurement along $L(\lambda, u)$ is denoted $g(\lambda, u)$, and the angle between $L(\lambda, u)$ and the line that connects $\underline{a}(\lambda)$ to the rotation center is called γ . Angle γ is measured positively in the counter-clockwise rotation, as shown in Fig. 1, so that $u = D\gamma$.

The CT measurements are also identified using parallel-beam coordinates, as shown in Fig. 2. In these coordinates, each ray is described by an angle θ and a signed distance s . Vector $\underline{\theta}^\perp = (-\sin\theta, \cos\theta)$ gives the direction of the ray, from source to detector, and s expresses how far the ray is from the origin in the direction of $\underline{\theta} = (\cos\theta, \sin\theta)$. The link between (θ, s) and (λ, γ) is

$$\theta = \lambda + \pi/2 - \gamma, \quad s = R_0 \sin \gamma. \quad (2)$$

The scanned object is inside a disk centered on the origin within the region delimited by the source trajectory. This disk is called the field-of-view (FOV) and its radius is $r_{\text{FOV}} < R_0$. Points within the FOV are identified by Cartesian coordinates, x and y . Reconstruction is performed on a finite set of points called (x_k, y_l) , where k and l are indices. These points are uniformly distributed in x and y . Throughout the paper, the same sampling distance is used in both x and y . This distance is denoted as Δ , so that $x_k = k \Delta$ and $y_l = l \Delta$. The number of samples in x is N_x and that in y is N_y . A square pixel of width Δ can be associated with each point (x_k, y_l) ; this pixel is centered on (x_k, y_l) . The samples obtained by varying k while keeping l fixed are said to form a row of samples. Similarly, the samples obtained by varying l while keeping k fixed form a column of samples.

Finally, the linear attenuation of x-rays is denoted as $f(x, y)$. Subsections 2.B–2.D present the link between $f(x_k, y_l)$ and the CT measurements for the three linear interpolation models that we compare.

2.B. Joseph's Method

The method of Joseph models each measurement as a straight line integral and approximates the integral along each

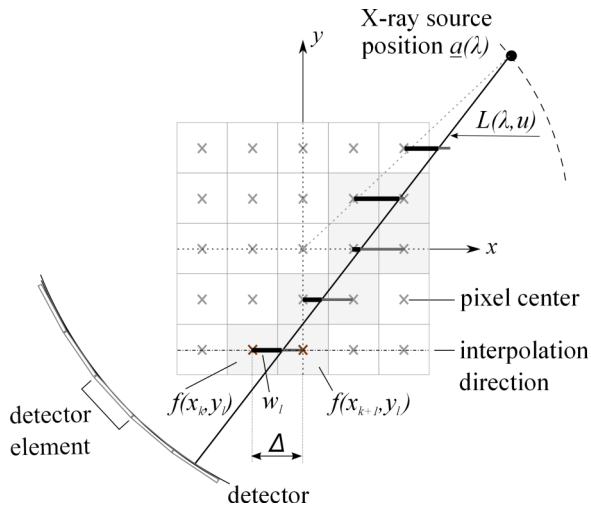


FIG. 3. Geometrical description of Joseph's method for $L(\lambda, u)$ more parallel to the y -axis than the x -axis, i.e., for $|\cos\theta| > 1/\sqrt{2}$. The measurement along such a line is created with linear interpolation in x and summation in y .

line either as a summation in x or in y depending on the direction of the line. This concept allows all computations to be done using a simple 1D interpolation. When the summation is in x (alternatively y), the interpolation is in y (respectively, x). Linear interpolation is used, and the summation direction is chosen according to angle θ in Eq. (2). When $|\cos\theta| > 1/\sqrt{2}$, the line is more parallel to the y -axis than the x -axis and the summation is in y ; otherwise, it is in x .

Figure 3 illustrates the concept for a case where the summation is in y . For each l , there is an intersection between $L(\lambda, u)$ and the line of coordinate y_l , and there is an index $k(l)$ such that this intersection is between $x_{k(l)}$ and $x_{k(l)+1}$ in x . Let w_l be the distance in x between the intersection and $x_{k(l)}$. Then, the underlying formula for Joseph's method can be expressed as

$$g(\lambda, u) \simeq \frac{\Delta}{|\cos\theta|} \cdot \sum_l \left\{ \frac{\Delta - w_l}{\Delta} f(x_{k(l)}, y_l) + \frac{w_l}{\Delta} f(x_{k(l)+1}, y_l) \right\}. \quad (3)$$

This formula is applied with $f(x_{k(l)}, y_l) = 0$ whenever $x_{k(l)}$ is outside the range of available samples and the same for $f(x_{k(l)+1}, y_l)$. The scaling factor in front of the summation is the Jacobian that accounts for the summation being performed in y instead of along the line.

The formula for the case where the summation is in x instead of y is very similar to Eq. (3). Basically, the summation is in k instead of l , l becomes an index depending on k , w_l is transformed into a distance, h_k , in y , and the scaling factor in front of the summation becomes $\Delta/|\sin\theta|$.

An important aspect in our description of Joseph's method is that the direction of summation may change within any given projection. An alternative would be to use the same direction of summation for all rays within the view. Since Joseph's method was truly only described for parallel-beam data, there is no consensus on what Joseph's method is for fan-beam data. Intuitively, a better accuracy may be expected if the

direction of summation is individually selected for each ray, particularly for geometries with a high magnification factor.

2.C. Distance-driven method

The distance-driven method is very similar to Joseph's method except for the key aspect that it accounts for the finite size of the detector pixel. As in Joseph's method, each measurement is created using a summation in x or y , but the summation direction is the same for all rays that are within a same view. If $|\sin\lambda| > 1/\sqrt{2}$, the summation is in y ; otherwise, it is in x . Once a summation direction has been chosen, say in y , the finite size of the detector pixel is accounted for using integration over the projected length of the detector pixel on each row of samples. If the summation direction was in x , the projected length would be identified on the columns of samples.

Figure 4 illustrates the concept for a case where the summation is in y . To create the measurement associated with a given detector pixel, we start by drawing the two lines that connect the source position with the edges of the detector pixel. For each l , these two lines intersect the line of coordinate y_l at two locations in x , called $q_1(l)$ and $q_2(l)$, with $q_1(l) < q_2(l)$. These two locations define the projected length of the detector pixel over which integration is to be carried out. This integration is performed in x using a nearest-neighbor interpolation model for representation of $f(x, y_l)$. The result is

$$g(\lambda, u) \simeq \frac{\Delta}{|\cos\theta|} \sum_l \left\{ \sum_k \frac{d_{k,l}}{q_2(l) - q_1(l)} f(x_k, y_l) \right\}, \quad (4)$$

where $d_{k,l}$ is the length of the overlap between the interval $[q_1(l), q_2(l)]$ and the interval $[x_k - \Delta/2, x_k + \Delta/2]$. If there is no overlap, then $d_{k,l} = 0$. The scaling factor in front of the summation in l is the same as in Joseph's method and has the same meaning. By definition, the summation over k in

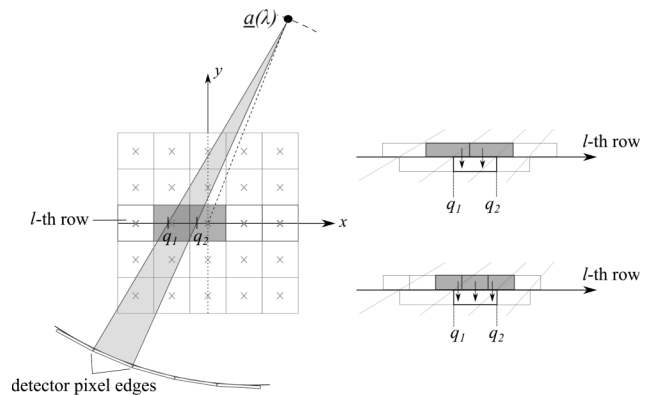


FIG. 4. Geometrical description of the distance-driven method in the case where $|\sin(\lambda)| > |\cos(\lambda)|$. (left) The measurement is created using summation in y with the contribution at each row position defined using integration over the projected length of the detector pixel, indicated as $[q_1, q_2]$. (right) The number of samples along the row that is involved in the integration varies with Δ , as well as q_1 and q_2 . The upper drawing shows a zoomed view for a situation where two samples are involved, whereas three samplings are involved in the lower drawing.

Eq. (4) only involves a few terms, but the exact number of terms depends on Δ as well as on l , λ , u , and the detector pixel size. The drawings on the right side in Fig. 4 show how the number of terms may vary with the sampling in x for our particular example.

From an implementation viewpoint, a preferred approach for the distance-driven method may be to perform the computations for all u values at once for each λ and each l , instead of summing on l before looping on the u values. Such an approach offers advantages in terms of cache memory usage, since values close to each other in memory can be used at the same time. The same concept can also be used for Joseph's method.

2.D. Bilinear method

Like in Joseph's method, the bilinear method models each measurement as a straight line integral. However, it does not require the selection of a preferred Cartesian direction, which maybe better for some rays. The concept is as follows: (i) use bilinear interpolation to estimate the value of f at every position along the measurement line and (ii) integrate the estimated values. The bilinear method was introduced by Kak and Slaney (Ref. 66, Section 7.4) who suggested an approximate implementation: bilinear interpolation to get f at a finite number of points along the line, followed by summation. To our knowledge, the bilinear method was never tested without approximation.

The parameters in the bilinear method are again the values of f at positions (x_k, y_l) . For convenience, these values are denoted here as c_{kl} . Let

$$b_1(t) = \begin{cases} 1 - |t|, & \text{if } |t| < 1 \\ 0, & \text{otherwise} \end{cases} \quad (5)$$

be the B-spline of order 1 and let $b(x, y) = b_1(x) b_1(y)$. From $b(x, y)$, we can write the estimate $f_a(x, y)$ of $f(x, y)$ that results from bilinear interpolation as

$$f_a(x, y) = \sum_{k,l} c_{kl} \cdot b\left(\frac{x - x_k}{\Delta}, \frac{y - y_l}{\Delta}\right). \quad (6)$$

Using this equation for f_a with the parallel-beam coordinates of Eq. (2), each line integral can be estimated as

$$g(\lambda, u) \approx \sum_{k,l} c_{kl} \cdot r(\theta, (s - x_k \cos \theta - y_l \sin \theta) / \Delta). \quad (7)$$

Equation (7) was used to implement the bilinear method with no approximation using the expression for $r(\theta, s)$ below. See Fig. 5 (left) for an illustration.

Conceptually, $r(\theta, s)$ is the Radon transform of $b(x, y)$. From Ref. 59, this transform can be expressed as

$$r(\theta, s) = \sum_{i=0}^2 \sum_{j=0}^2 (-1)^{i+j} \binom{2}{i} \binom{2}{j} \cdot \frac{[s + (1-i) \cdot h_1(\theta) + (1-j) \cdot h_2(\theta)]_+^3}{(3)!(h_1(\theta) h_2(\theta))^2}, \quad (8)$$

where the one-sided power function $[x]_+^3$ is defined as

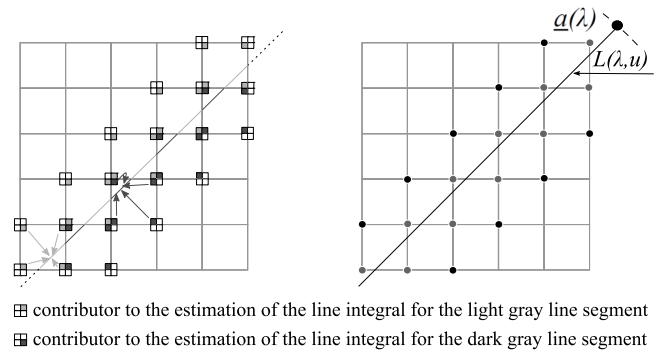


Fig. 5. (left) Illustration of the bilinear method: the line is split into segments, each of which falls between four samples; these samples are used with bilinear interpolation to get the function at every location on the segment; then the results from all segments are integrated. (right) Comparison of samples used by Joseph's method (gray dots) and the bilinear method (gray and black dots).

$$x_+^3 = \begin{cases} x^3, & x \geq 0 \\ 0, & \text{otherwise} \end{cases} \quad (9)$$

and where $h_1(\theta) = \frac{1}{2} |\cos \theta|$ and $h_2(\theta) = \frac{1}{2} |\sin \theta|$. Note that $g(\theta, s)$ reduces to $b_1(s)$ when θ is a multiple of $\pi/2$.

The bilinear method may be best implemented using a loop over k and l before u for each λ . An important computational burden lies in the computation of $r(\theta, s)$, but this burden can be largely decreased using interpolation with a look-up table. However, such a table was not used, as our primary goal was to assess the best possible performance with the bilinear method. Note also that implementation using the approximation suggested in (Ref. 66, Section 7.4) may be fast using GPU features.

2.E. Comparative discussion

All three methods may be classified as linear interpolation methods. However, the manner in which the linear interpolation is applied is fundamentally different from one method to the other, which can impact image quality and computational cost in iterative reconstruction.

A first fundamental difference is about the utilization of pixel values. Figure 6 (top) illustrates a situation where the pixel size is small relative to the separation between the rays. Such a situation yields imbalances in Joseph's method in the sense that some pixel values appear under-utilized in comparison with others. In the illustration, it can be seen that the interpolation between pixels b and c is not required in this particular view. If Δ were much smaller or if the rays were more separated, it could even be that some pixels would play no role in modeling the measurements in this view. This observation may be seen as an undesirable feature of Joseph's method. Given its definition, the bilinear method exhibits the same feature, albeit not with the same importance for a given pixel size, since the size of the pixel in both x and y matters in that method. On the other hand, the distance-driven method is not similarly affected.

A second fundamental difference is in the number of pixels involved in the interpolation procedure. Unlike with the other

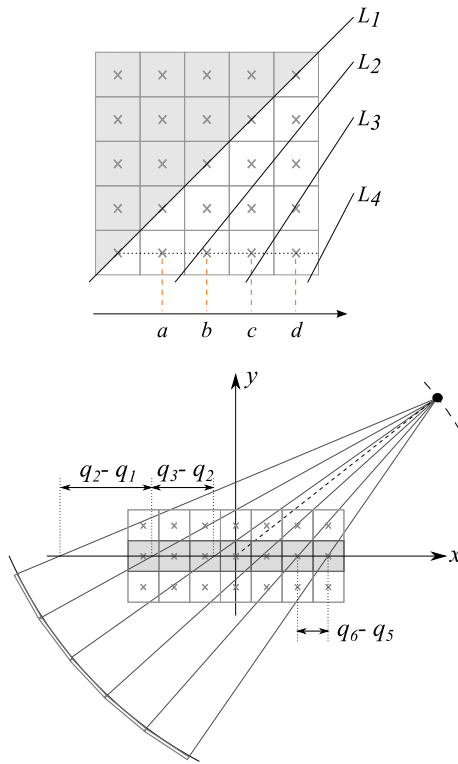


FIG. 6. Geometrical features affecting the forward projection model. (top) The pixels may be under-utilized with Joseph's method; for example, in this view, no interpolation is required between pixels b and c . (bottom) The interpolation lengths can become quite large with the distance-driven approach; for example, in this view, $q_2 - q_1$ is much larger for the negative values of u than for the positive ones.

two methods, this number can vary a lot in the distance-driven method. Figure 6 (bottom) illustrates a high magnification geometry with λ close to $\pi/4$. It can then be seen that the interpolation length, $q_2 - q_1$, can become quite large. Such imbalances may negatively impact the computational effort as well as the image quality. Additionally, there is also a significant difference in the number of pixels involved between Joseph's method and the bilinear method, as illustrated in Fig. 5 (right).

A third fundamental difference is in the potential accuracy of the interpolation for the views where $|\tan \lambda|$ is close to 1. The concept of summing in x or y instead of along the ray appears suboptimal in these views. Because they sum in x or y , Joseph's method and the distance-driven approach could be less accurate than the bilinear method, which sums along the ray. Note, however, that by allowing the summation direction to change from ray to ray within a view, Joseph's method may be less exposed to this issue than the distance-driven approach.

3. EXPERIMENTAL COMPARISON SETUP

This section presents the choices made for the comparison of the forward projection models, which include the image formation process, data acquisition geometries, image parameters, phantom selection, and data simulation.

3.A. Image formation process

Let c be the vector of unknown image values, which were called $f(x_k, y_l)$ in Sec. 2, let g be the vector grouping the CT measurements, and let A be the matrix that links c to the CT measurements. Now, let $\{\sigma_m, u_m, v_m\}$ represent the singular value decomposition of A . Given that A is a discrete model of the Radon transform, the singular vectors are known to be progressively associated with finer details as m increases. Moreover, it is known that the singular values rapidly decrease with m , so that fine details recovery is more sensitive to noise. Different forward projection models yield singular vectors with different features and as well as different stability for the inclusion of these features in the reconstruction.

We compare the forward projection models using a summary of information included in the singular value decomposition of A . This summary is defined as a sequence of images $c^{(n)}$ that gradually include more and more information from the singular value decomposition of A for a given data set g ,

$$c^{(n)} = \sum_m f^{(n)}(\sigma_m) \frac{(u_m^T g)}{\sigma_m} v_m, \quad (10)$$

where $f^{(n)}(\sigma_m)$ converges toward unity with n . Increasing n amounts to trying to sharpen the reconstruction, $c^{(n)}$, by increasing the weight given to singular vectors that include fine details. Depending on the forward projection model, some of these details may however not be desirable, yielding artifacts similar to discretization errors. Also, they may be too sensitive to noise for reliable usage. When $f_n(\sigma_m) = 1$, $c^{(n)}$ becomes the result of applying the Moore–Penrose inverse of A to g , which, in tomography, is highly sensitive to noise in g .

To circumvent the computationally-demanding issue of determining the singular value decomposition of A , the sequence of images $c^{(n)}$ was created indirectly, using Landweber iterations with $c^{(0)}$ chosen as the zero vector

$$c^{(n+1)} = c^{(n)} + \beta \cdot A^T (g - A c^{(n)}). \quad (11)$$

These iterations are equivalent to using Eq. (10) with

$$f^{(n)}(\sigma_m) = 1 - (1 - \beta \sigma_m^2)^{n+1}. \quad (12)$$

Parameter β was chosen as 0.9 times $2/\sigma_{\max}^2$, where σ_{\max} is the maximum singular value of A , estimated using five iterations of the power method.⁷¹

Most of our comparison results are reported as a function of a figure-of-merit for resolution that serves as a surrogate for n . To achieve this goal, the result from every fifth iteration was stored, starting from iteration 40 and stopping after 1000 iterations. The first 40 iterations were discarded because the resolution was too low for these images to be of interest. At $n = 40$, $f^{(n)}(\sigma_m)$ is essentially equal to unity for $\sigma_m > 0.3 \sigma_{\max}$ and smoothly decreases toward zero for the other singular values. As n increases beyond $n = 40$, $f^{(n)}(\sigma_m)$ smoothly converges toward unity for each index m .

3.B. Geometrical settings

Our comparative study includes 16 different geometrical (parametric) settings that are the representative of

contemporary CT scans. We differentiate between moderate pixel size (MPS) and small pixel size (SPS), low and high magnification, full-scan and short-scan, and FFS off and FFS on. These aspects allow us to probe various features of the forward projection models. For example, as discussed earlier, the pixel size is an important factor for both Joseph's and the bilinear method, and high magnification may impact the distance-driven method more than the other two methods. Also, the data redundancies that are present within a full-scan may yield artifact/noise cancellations that are not feasible with a short-scan, and FFS off or on further affects data sampling.

The comparison is divided into two subsets based on the pixel size. The same label concept is used for the moderate and the small pixel size as shown in Fig. 7. Thus, each geometrical setting has an associated number together with an abbreviation denoting the pixel size. For example, G1-MPS denotes geometrical setting 1 with moderate pixel size, where geometrical setting *G1* is defined using low magnification, full-scan mode and FFS off.

All data simulation and image reconstruction parameters are summarized in Table I. The grid of image pixels was always centered on the origin and the computations were only carried out over the pixels that were within the circle of radius $r_{\text{FOV}} = 13$ cm. To better appreciate our selection for Δ , note that modern CT scanners typically offer 512×512 images with pixels distributed over a user-selected region, the maximum length of which is 50 cm. At maximum length, the pixel size is about 0.1 cm, whereas a pixel size of 0.075 cm would correspond to selecting a region of 38 cm and a pixel size

TABLE I. Data simulation and image reconstruction parameters. MPS, SPS, and FFS stand for the moderate pixel size, small pixel size, and flying focal spot, respectively. Poisson noise is added to the data assuming that N_{in} photons are emitted toward each detector pixel; N_{in} is adjusted with the number of projections to have the same total exposure in all geometries.

Image size	351 × 351 (MPS) 701 × 701 (SPS)
Δ	0.075 cm (MPS) 0.0375 cm (SPS)
R_0	57 cm (low magnification) 36 cm (high magnification)
Detector width at isocenter	0.075 cm
Detector height at isocenter	0.075 cm
Number of detector pixels	380
Detector pixel offset	1/4 (FFS off) 1/8 (FFS on)
Number of projections (N_{λ})	1200 (full scan, FFS off) 2400 (full scan, FFS on) 800 (short scan, FFS off) 1600 (short scan, FFS on)
N_{in}	$(1200/N_{\lambda}) \times 60,000$

of 0.0375 cm to selecting a region of 19 cm. The size of 0.075 cm is a representative of abdominal and chest scans of an average-size patient, whereas the smaller size of 0.0375 cm is a representative of head or heart-focused scans. Parameters Δu and D were chosen so that the same resolution is achieved at the isocenter in all geometries. The low magnification represents a classical head/body CT scanner, whereas the high magnification represents a head-dedicated CT scanner.⁷² For the full scan, $[\lambda_s, \lambda_e] = [0, 2\pi]$ was used. For the short scan, the start angle was $\lambda_s = 0$ and the end angle was $\lambda_e = 4\pi/3$. Thus, the number of projections on a short-scan was 2/3 of that on a full-scan. When using the flying focal spot, the number of projections was doubled, as in the scanner.

3.C. Phantom selection and data simulation

Our evaluations were carried out using the FORBILD head phantom,⁷³ which has been accepted as a standard in the CT community due to its simple yet challenging definition. Note that this phantom is 3D. In this work, we only analyzed the central axial slice through it, a description of which can be found in Ref. 74.

Data simulation was carried out in 3D, as a CT scan with one detector row of finite nonzero thickness, using a proprietary software. The simulation model included a subsampling of the x-ray tube focal spot, a subsampling of the detector element, and a subsampling of each source position. These settings allowed us to model the shift-variant effect of the x-ray tube anode angle on resolution, to model the blurring that results from continuous x-ray emission, and to model the blurring that results from the finite size of the focal spot and detector elements. More specifically, a 3×3 subsampling was used for the focal spot as well as for each detector element, and each view was simulated using 5 subsource positions. All subsampling positions were uniformly distributed. In total,

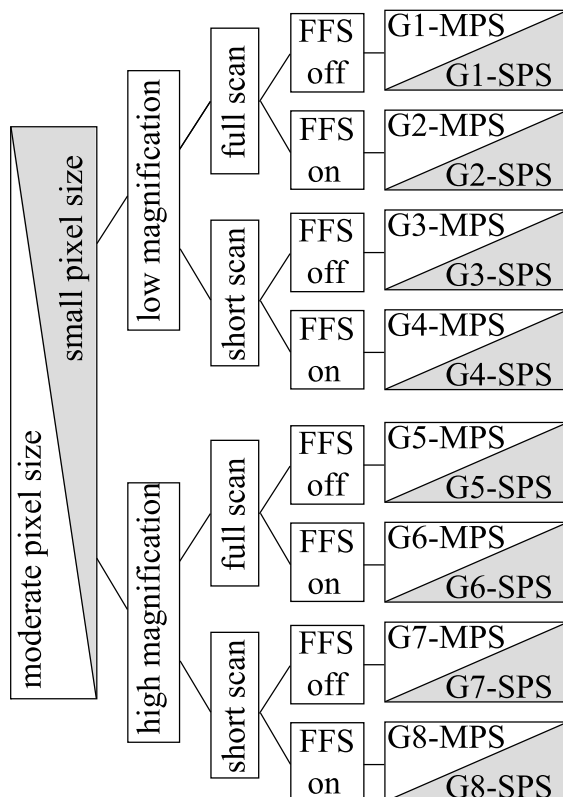


FIG. 7. Label concept for the 16 geometrical settings.

each CT measurement was thus simulated as an average of 405 line integrals. The computation of each line integral was based on analytical expressions, and the average was performed before applying the logarithm. For further information and a visual description of our data simulation model, see Ref. 75. The x-ray tube focal spot size was 0.12×0.09 cm, and the anode angle was 7° . For scans with FFS on, the shift was $|\delta(\lambda)| = 0.0415$ cm for both magnifications, as suggested in Ref. 76.

All evaluations with noise involved 50 noise realizations for each geometrical setting. Poisson noise was used with a fixed number of incoming photons, N_{in} , for each ray; see Table I. This number was changed with the number of projections to ensure that the total exposure was always the same. Recall that the attenuation values in the FORBILD phantom are given as a fraction of the attenuation value of water. To work with physical units, all attenuation values in the phantom were scaled with a factor of 0.183/cm, which represents the linear attenuation coefficient of water at 80 keV. Note that N_{in} was the same for both low and high magnification, and noise simulation did not include a compensating bowtie filter nor tube current modulation.

4. QUANTITATIVE COMPARISON: METRICS

The impact of the forward projection models was quantitatively evaluated using a number of metrics that are described in this section. Basic metrics covering resolution, computational cost, bias, and noise propagation were used as well as metrics related to the task-based assessment.

4.A. Spatial resolution evaluation

Spatial resolution was evaluated using the modulation transfer function (MTF), relying on the fact that the iterations $c^{(n)}$ linearly depend on the CT data, g . This function was obtained using a phantom that consists only of the large low contrast ellipse within the FORBILD head phantom; see Fig. 10 (left). For any reconstruction of this phantom, an edge profile that gives the reconstructed values as a function of the distance from the ellipse was computed. Then, the MTF was obtained as the Fourier transform of the differentiated edge profile. To apply this last step, the numerous samples forming the edge profile were first grouped together in bins of width $\Delta/4$ that were sampled with a step of $\Delta/4$. For display and analysis, all MTF curves were normalized so that the value at zero frequency was equal to one. Since the reconstruction method investigated in this paper is linear, the above procedure is suitable to evaluate the spatial resolution achieved within the neighborhood of the large low-contrast ellipse.

In each geometry, there were slight variations in resolution from one forward projection model to another. These effects are illustrated in Figs. 8 and 9. The first figure shows that the MTF curve at a fixed number of iterations is not always the same for each forward projection model. The second figure shows the frequency at which the MTF reaches a value of 0.5, which is called $\nu_{0.5}$, as a function of the number of iterations.

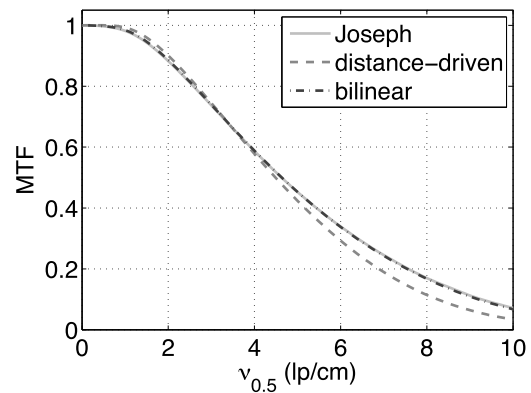


FIG. 8. MTF curve for the geometrical setting G1-SPS after 201 Landweber iterations for all three forward projection models.

Both figures are for Geometry G1-SPS. To account for these differences in resolution, all figures of merit are displayed as a function of $\nu_{0.5}$. Note that the differences were more pronounced in the SPS geometries than the MPS ones.

4.B. Computational cost

Computational cost evaluation was limited to the application of the matrix A that represents the forward projection model. That is, the additional effort needed to create the elements of this matrix was not included in our evaluations. This effort strongly depends on implementation optimization, which was out of the scope of this work. In our nonoptimized implementation, the bilinear method always required much more effort for the computation of the elements of A , primarily because no look-up table was used. Also, computing the elements of A took more time with the distance-driven method than with Joseph's method, particularly for the SPS geometries.

Our metric for computational cost as a function of $\nu_{0.5}$ was the number of iterations needed to reach this MTF frequency times a factor adjusting for differences in the number of nonzero elements in A , which reflects the difference in computational cost associated with the application of A . Let

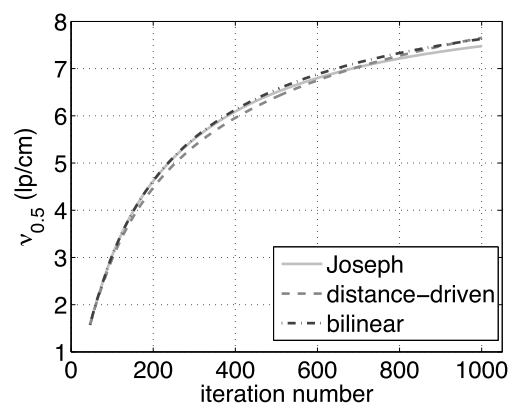


FIG. 9. Frequency at which the MTF reaches a value of 0.5, $\nu_{0.5}$, as a function of the iteration number in the geometrical setting G1-SPS for all three forward projection models.



FIG. 10. (left) Phantom used for the computation of the MTF curves. (middle) Mask used for the evaluation of bias in noise-free reconstructions. (right) Region used for the evaluation of the mean standard deviation and the correlation coefficient in reconstructions from noisy data; this region is the large rectangle with white borders.

N_J , N_D , and N_B be this number for the Joseph, distance-driven, and bilinear methods, respectively. The adjustment factor was equal to one for Joseph's method, to N_D/N_J for the distance-driven approach, and to N_B/N_J for the bilinear method. The average values for these factors were $N_D/N_J = 1.05$ and $N_B/N_J = 1.52$ in the MPS geometries and $N_D/N_J = 1.60$ and $N_B/N_J = 1.53$ in the SPS geometries.

4.C. Bias evaluation

Bias was evaluated as a mean reconstruction error over pixels that are away from edges and share a common attenuation value in the ground truth image. This set of pixels was identified using a mask that is shown in Fig. 10 (middle). To create this mask, the ground truth image was convolved with a square box function. Then, the convolved image was compared with the original phantom and the mask was defined as the set of pixels that showed the same attenuation value of 50 HU in both images. The width of the box function was equal to 9 pixels. This width was carefully selected so as to avoid interference with resolution effects.

The reconstruction error for each pixel was simply defined as the difference between the reconstructed value and the true attenuation value. The mean of the square of these differences was evaluated over all pixels within the mask, and the square root of this mean was used as the definition for the bias. Later on, we also refer to the bias as the RMSE (root-mean-squared-error).

4.D. Noise evaluation

Due to statistical noise in the data, any reconstructed image needs to be seen as one realization of a multivariate random variable. Given that the reconstruction algorithm used here is linear and that a large number of photons were used in our data simulation, this variable was essentially normally distributed. Thus, effects due to noise could be quantified by analyzing the standard deviation in the pixel value as well as the correlations between pixels. Because 50 noise realizations is not a number large enough to avoid significant statistical errors in the evaluation of pixel standard deviation and correlation between pixels, mean values were used as final metrics. These mean values are described below.

4.D.1. Mean standard deviation

First, the sample variance formula was invoked with the 50 noise realizations to estimate the pixel variance for each pixel within the rectangular region shown in Fig. 10 (right). Next, all obtained values were averaged together, and a square root was taken. The outcome of this square root was defined as the mean standard deviation. The rectangular region was of size 125×112 for the MPS geometries and of size 250×224 for the SPS geometries. In both cases, the box was centered on location $(x, y) = (-0.8625, -2.55)$ cm. The statistical accuracy of our mean standard deviation was very high. For example, in geometry G1, the utilization of another set of 50 noise realizations yields less than 1% difference in the mean standard deviation.

4.D.2. Mean correlation coefficient

By definition, the correlation coefficient is a quantity that involves two pixels. Our evaluations were focused on correlations between pixels that are adjacent to each other, either in x , in y , or at 45° . The procedure to obtain a mean correlation coefficient in x was as follows. First, we identified all pairs of pixels that are adjacent to each other in x within the rectangular region shown in Fig. 10 (right), which is the same region as that used for the evaluation of the mean standard deviation. Then, the formula for the sample correlation coefficient was invoked with the 50 noise realizations to obtain an estimate of the correlation coefficient for each of these pairs of pixels. Finally, all obtained values were averaged together. The procedure to obtain a mean correlation coefficient in y or at 45° was the same as that used for the mean correlation coefficient in x , except for the identification of pairs of pixels. The statistical accuracy of our mean correlation coefficients was found to be similar to that of our mean standard deviation.

4.E. Task-based assessment

Common tasks include classification, detection, and estimation.⁷⁷ We considered an estimation task which was defined as the evaluation of the background value at various locations within the phantom. The estimator for the background value was the mean pixel value within a region-of-interest (ROI). A total of 11 locations were chosen for the ROI. These locations are shown in Fig. 11 with individual numerical labels running from 1 to 11. Table II gives the center position, (x_c, y_c) , for each ROI. The size of the ROI was 11×11 pixels in the MPS case and 21×21 pixels in the SPS case.

The mean pixel value, called m , was evaluated at a same resolution level for each forward projection method, namely $v_{0.5} = 4.75/\text{cm}$. In addition to evaluating the background value, we also estimated the square root of the geometry-averaged variance of m . This quantity, called σ , assesses how m varies with the quantum noise, in average over the geometries. An insightful expression for σ is

$$\sigma = \sqrt{e^T C e}, \quad (13)$$

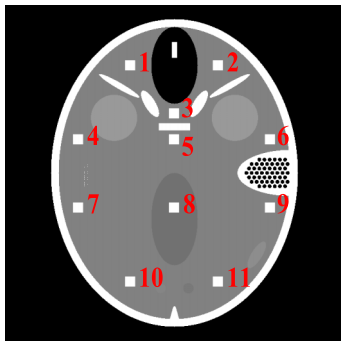


FIG. 11. Arrangement and labeling of 11 ROIs used for the estimation task, which consists in evaluating the background value at various locations in the phantom.

where C is the covariance matrix for the pixels within the ROI, as obtained after averaging over the geometries, and e is a vector with entries all equal to $1/N_{\text{pix}}$ with N_{pix} being the number of pixels in the ROI. Unlike m , this quantity is independent of the bias. It allows singling out differences in the noise behavior. To get an estimate of σ , we replaced C by the average of the sample covariance matrices available for m in each geometry; these matrices were obtained from the 50 noise realizations. The outcome is the same as computing the square root of the geometry-averaged sample variance of m .

5. QUANTITATIVE COMPARISON: RESULTS

By design, our analysis generated a large amount of data, including $3 \times 8 \times 2$ curves for each basic metric (three forward projection models, eight geometries, and two pixel sizes). Each curve showed the metric behavior as a function of $v_{0.5}$, and there were six basic metrics (computational cost, bias, mean pixel standard deviation, and mean pixel correlation coefficient in x , in y , and at 45°). These results, as well as those obtained for the task-based assessment, are presented hereafter in a condensed format, using the abbreviations “J,” “D,” and “B” to refer to Joseph’s method, the distance-driven method, and the bilinear method, respectively, and also using the abbreviation MPS or SPS to clarify which pixel size a result corresponds to. Beforehand, some examples of reconstructions are provided so that the results can be partly linked with a visual impression.

5.A. Visual appearance of reconstructions

Figures 12 and 13 show reconstructions obtained in geometry G1-MPS and G1-SPS, respectively. Each figure includes noise-free and noisy reconstructions. Note that the grayscale window is more compressed for the noise-free

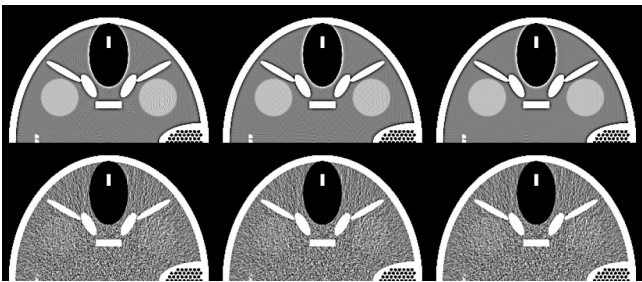


FIG. 12. (left) Noise-free and noisy reconstructions obtained in geometry G1-MPS after 251 Landweber iterations: (first column) Joseph’s method, (middle column) the distance-driven method, (third column) the bilinear method. Noiseless images: $c/w = 50/40$ HU; noisy images: $c/w = 50/200$ HU.

reconstructions to emphasize the discretization errors. Also, only the upper portion (region $y > 0$) of the reconstructions is shown, as the other portion would not convey more information.

In G1-MPS, the noiseless reconstructions show that, unlike method B, methods J and D both yield discretization errors around the $\pm 45^\circ$ directions. However, the magnitude of all discretization errors is fairly small. In the presence of noise, the discretization errors are difficult to see and so are other possible differences between the three forward projection models.

In G1-SPS, methods J and B both yield more discretization errors than method D, but the magnitude of the discretization errors remain fairly small, so that it is still difficult to distinguish these differences in the presence of noise. Unlike in G1-MPS though, method D visibly yields a different noise structure in comparison with the other two methods.

5.B. Display concept for the basic metrics

Results corresponding to different metrics or different pixel sizes are shown in separate figures. To minimize the number of figures, the results obtained for all three forward projection models are always incorporated together in each figure. Three different tones of gray are used for this purpose: light gray for method J, medium gray for method D, and dark gray for method B. Moreover, the dependence over the 8 geometries is summarized by its first two moments when the variations according to $v_{0.5}$ are more prominent, which is the case for the computational cost and the noise metrics. Similarly, the dependence over $v_{0.5}$ is summarized by its first two moments when the variations according to the geometries are more prominent which is the case for the bias. Hence, for the computational cost and the noise metrics, the first moment is the mean value over the geometries as a function of $v_{0.5}$, which is provided together with standard deviation

TABLE II. Position (x_c, y_c) for the center of each ROI (in cm).

ROI	1	2	3	4	5	6	7	8	9	10	11
x_c	−3.4125	3.4125	0	−7.4625	0	7.4625	−7.4625	0	7.4625	−3.4125	3.4125
y_c	8.4375	8.4375	4.6875	2.6625	2.6625	2.6625	−2.6625	−2.6625	−2.6625	−8.4375	−8.4375

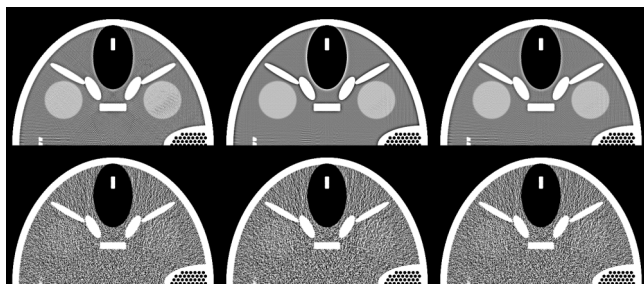


FIG. 13. Same reconstructions and arrangement as in Fig. 12 but for geometry G1-SPS.

bars (second moment) at occasional values of $\nu_{0.5}$ conveying the dependence over the geometries. For the moderate pixel size, the frequency range is $\nu_{0.5} \in [1.55, 6.29]/\text{cm}$ and the average is always over all eight geometries. For the small pixel size, two frequency ranges, $\nu_{0.5} \in [1.58, 5.43]/\text{cm}$ and $\nu_{0.5} \in (5.43, 6.79]/\text{cm}$, are involved because the maximum frequency reached in G3-SPS and G7-SPS was lower than that reached in the other SPS cases. For the bias metric, the first moment is the mean value over $\nu_{0.5} \in [1.58, 5.43]/\text{cm}$, which is provided in the form of a bar plot with error bars (second moment) that convey the dependence over $\nu_{0.5}$.

5.C. Results for the basic metrics

Figure 14 compares the three forward projection models in terms of computational effort. As can be seen, method J always

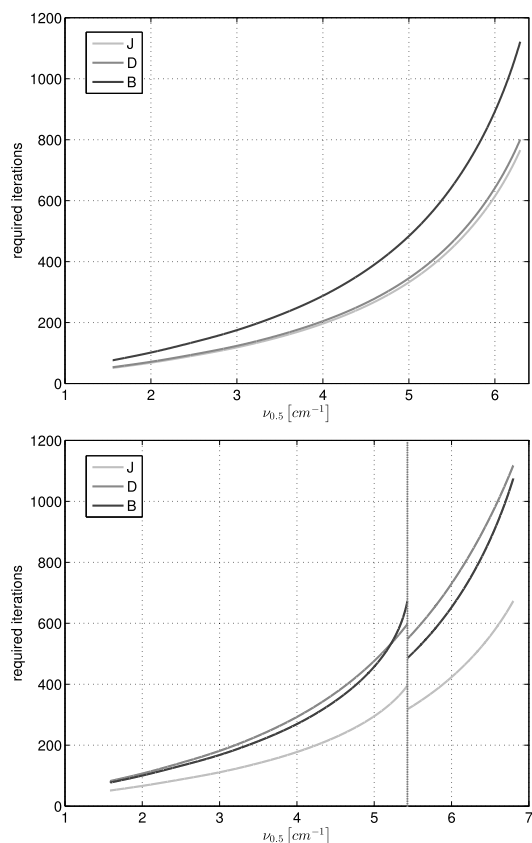


FIG. 14. Computational effort as a function of $\nu_{0.5}$. Only the first summary plot is shown. (top) MPS. (bottom) SPS.

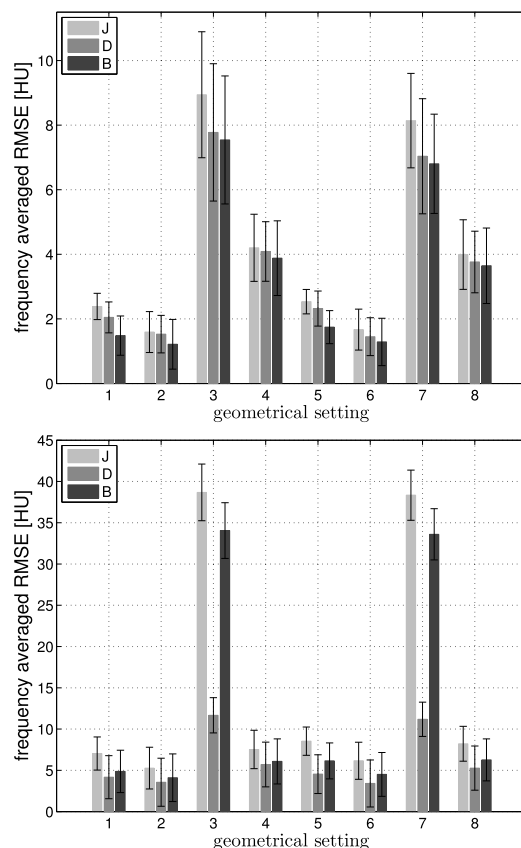


FIG. 15. Frequency-averaged RMSE for each geometry for MPS (top) and SPS (bottom).

required less effort. The increase in effort for method B varied between 45% and 70%. The increase in effort for method D was strongly dependent on the pixel size: it only was around 4% for MPS, but varied between 51% and 73% for SPS.

Figure 15 compares the methods in terms of bias. For both MPS and SPS, the frequency-averaged RMSE was clearly dependent on the geometry. The strongest effect was observed for geometries 3 and 7, namely the short-scans without FFS. These geometries are associated with fewer views which resulted in a higher bias. For MPS, the bias in geometry 3 and 7 was between 6.8 and 8.9 HU; for the other geometries the bias was always below 4.2 HU. Methods J and B consistently yield the highest and the lowest bias but no differences higher than 1.4 HU were observed. For SPS, the lower number of views in geometries 3 and 7 affected methods J and B much more than method D, with values as high as 38.7 HU for method J and 34.1 HU for method B, whereas the bias for method D was near 11.7 HU. In the other geometries, the bias was always below 8.5 HU. Also, method D consistently yields the lowest bias but the difference was always below 4.0 HU relative to method J and below 1.7 HU relative to method B. Last, the bias plots also show that the dependence on $\nu_{0.5}$ was fairly similar from one geometry to another; in average over the geometries, the standard deviation for the dependence on $\nu_{0.5}$ was below 1.1 HU for MPS and 2.8 HU for SPS.

Figure 16 compares the methods in terms of noise performance for MPS and SPS, respectively. Note that results

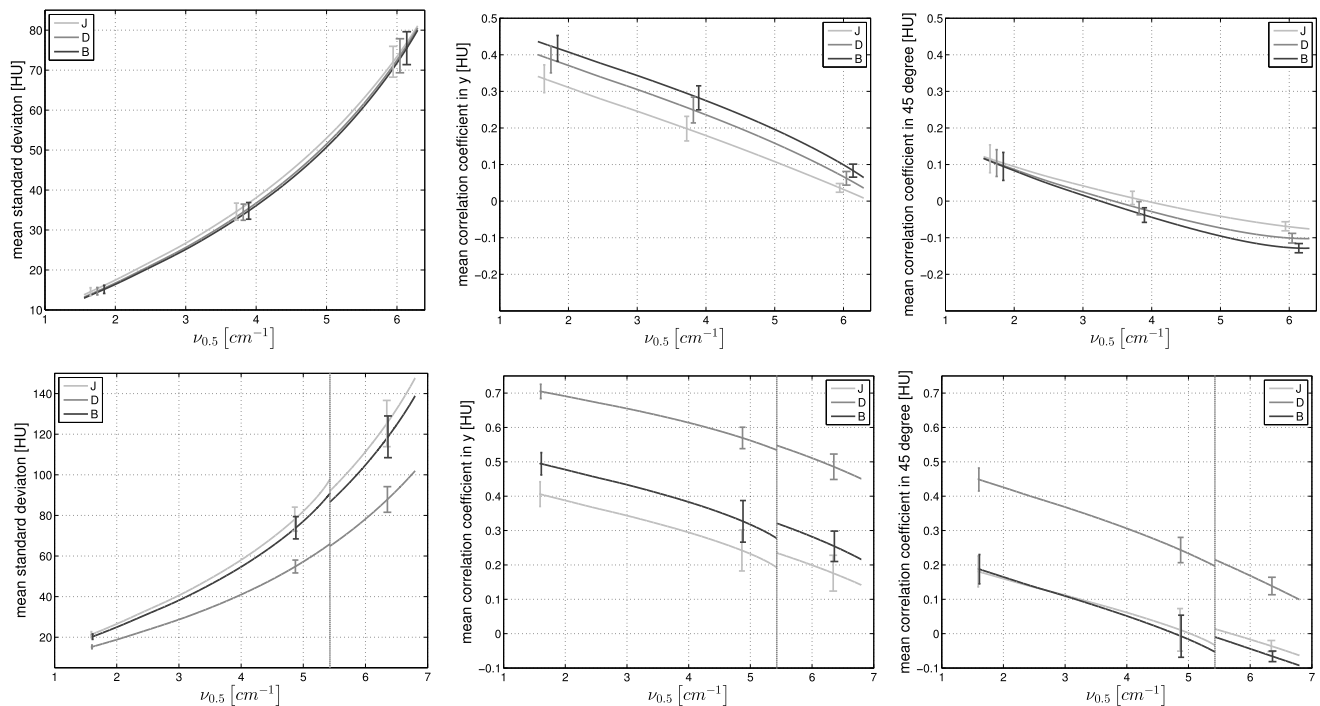


FIG. 16. Geometry-averaged metrics as a function of $\nu_{0.5}$ for (top plots) MPS and (bottom plots) SPS. From left to right: mean standard deviation, correlation coefficient in y , correlation coefficient at 45°.

for the correlation coefficient in x are not shown because they did not convey additional information. For MPS, the dependence of noise metrics on frequency and geometry was very similar for all methods. Differences of about 2 HU were observed in the mean standard deviation, with methods B and J always performing best and worst, respectively. Also, there were large differences in the correlation coefficient: method J yields less correlation between the pixel values than methods D and B, with differences as high as 0.05 and 0.1 compared to methods D and B, respectively. For SPS, the dependence of noise metrics on frequency and geometry was also observed to be very similar for all methods. However, differences as large as 40 HU were observed in the mean standard deviation, and methods D and J became the methods that always perform best and worst, respectively. Moreover, the differences in the correlation coefficient dramatically increased. A difference as large as 0.3 was observed between methods J and D. Also, unlike in MPS, method B created correlation levels that are much closer to those of method J than method D. Finally, the plots also show that, in the MPS case, the dependence on the geometry was similar for all methods and this dependence was relatively small: the dependence over the geometries was around 6% for the mean standard deviation, and the standard deviation over the geometries was never larger than 0.035 for the mean correlation coefficients. In the SPS case, the plots show a larger dependence on the geometry for methods J and B than for method D; the dependence however remains fairly small for all three methods: for the mean standard deviation, the dependence over the geometries was around 8% for method D and 1% to 2% higher for methods J and B; for the mean correlation coefficients, the standard deviation

over the geometries was always below 0.035 for method D and 0.06 for methods B and J.

5.D. Results for the estimation task

We only show the results obtained for all eight geometries in the MPS case. For the SPS case, we excluded the results obtained for geometries G3 and G7 because methods B and J yield a much larger bias than method D in these geometries (see Fig. 15). That is, in geometries G3 and G7, methods J and B should not be seen as competitive relative to method D. Also, including G3 and G7 would mask the SPS results for the other geometries.

The results obtained for m are compared using Bland–Altman plots. These plots include 4400 and 3300 points for the MPS and SPS cases, respectively, with each point corresponding to a different noise realization (of which there are 50), a different geometry, and a different ROI location. Figure 17 shows the Bland–Altman plots⁷⁸ in the MPS case (upper row) as well as in the SPS case (lower row). In each case, there are three plots: the first one compares method J to method D, the second one is for methods J and B, and the last one is for methods D and B. In each plot, three dashed lines highlight the mean value and the addition/subtraction of 1.96 times the standard deviation to the mean, as is commonly used. The Bland–Altman plots show that all forward projection methods perform very similarly for the selected estimation task. In the MPS case, the bias (mean difference) is negligible (<0.02 HU), and the difference between the estimated background value from one method to another is below 0.2 HU in 95% of scenarios. In the SPS

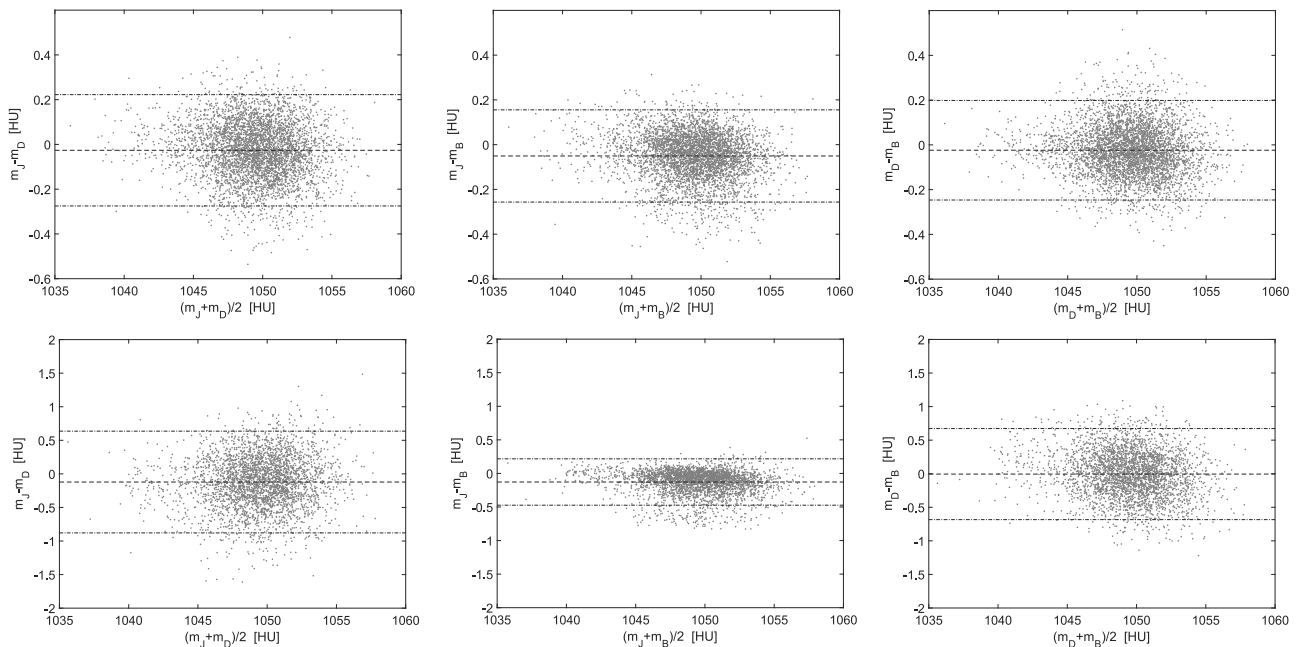


FIG. 17. Bland–Altman plots in the MPS case (upper row) and the SPS case (lower row). From left to right, the plots for methods J and D, methods J and B, and methods B and D. Each point in any of these plots corresponds to a different noise realization, a different geometry, and a different ROI location.

case, the bias is also negligible, and the difference between the estimated background value is still small although slightly larger; specifically it is below 0.7 HU in 95% of scenarios.

Tables III and IV compare the values obtained for σ_J , $\sigma_J - \sigma_D$, and $\sigma_J - \sigma_B$ at each ROI location, for the MPS and SPS cases, respectively. These values are given with their standard deviation and also the p -value for hypothesis testing on the differences of means. The standard deviations and the p -values were obtained using properties of the Wishart distribution^{79–81} together with application of the delta method and estimate plugins, all under the assumption that the pixels within the ROI follow a multivariate Gaussian distribution.⁸²

TABLE III. Estimated values of σ_J , $\sigma_J - \sigma_D$, and $\sigma_J - \sigma_B$ for each ROI in the MPS case, with standard deviation given between parentheses. See Eq. (13) for a definition of these quantities. The values are supplied with their standard deviation as well as the p -values for hypothesis testing on the difference of means. The statistically significant differences (p -value below the 0.01) are indicated with an asterisk.

ROI	MPS			p -value	
	σ_J	$\sigma_J - \sigma_D$	$\sigma_J - \sigma_B$	$\sigma_J - \sigma_D$	$\sigma_J - \sigma_B$
1	2.51 (0.09)	−0.012 (0.005)	−0.015 (0.003)	0.0105	0.0000*
2	2.37 (0.09)	−0.015 (0.005)	−0.011 (0.002)	0.0016*	0.0000*
3	2.46 (0.09)	−0.010 (0.003)	−0.012 (0.003)	0.0002*	0.0002*
4	2.16 (0.08)	−0.006 (0.004)	−0.008 (0.003)	0.1493	0.0014*
5	2.65 (0.10)	−0.012 (0.003)	−0.018 (0.004)	0.0001*	0.0000*
6	2.18 (0.08)	−0.016 (0.004)	−0.020 (0.003)	0.0002*	0.0000*
7	2.06 (0.07)	−0.011 (0.004)	−0.008 (0.003)	0.0054*	0.0053*
8	2.78 (0.10)	−0.008 (0.003)	−0.011 (0.003)	0.0096*	0.0009*
9	2.13 (0.08)	−0.005 (0.004)	−0.008 (0.002)	0.1703	0.0003*
10	2.24 (0.08)	−0.004 (0.005)	−0.008 (0.003)	0.3775	0.0012*
11	2.43 (0.09)	−0.017 (0.005)	−0.023 (0.003)	0.0005*	0.0000*

Table III shows that, in the MPS case, all differences in the value of σ are in favor of method J. Most of these differences are statistically significant, but they are relatively small ($<1\%$). On the other hand, as can be seen in Table IV, the differences are not anymore in favor of method J in the SPS case. However they remain fairly small, and most of them are not statistically significant. Note that methods J and B produced results that are systematically closer to each other than in the MPS case. Note also that the largest differences are observed at positions 6, 9, and 11: σ_D is, respectively, 2.0%, 1.6%, and 2.6% lower than σ_J at these locations, whereas the differences at other locations are below (or close to) 1%.

5.E. Summary discussion

Our results showed that the forward projection methods definitely yield differences in image characteristics as well as

TABLE IV. Same as in Table III but for the SPS case.

ROI	SPS			p -value	
	σ_J	$\sigma_J - \sigma_D$	$\sigma_J - \sigma_B$	$\sigma_J - \sigma_D$	$\sigma_J - \sigma_B$
1	2.55 (0.11)	0.026 (0.013)	0.004 (0.002)	0.0500	0.0948
2	2.36 (0.10)	−0.009 (0.014)	0.004 (0.002)	0.5166	0.0608
3	2.45 (0.10)	0.022 (0.015)	0.001 (0.003)	0.1378	0.7448
4	2.25 (0.10)	0.019 (0.013)	0.000 (0.002)	0.1371	0.9376
5	2.83 (0.12)	0.022 (0.014)	0.004 (0.003)	0.1350	0.2637
6	2.31 (0.10)	0.047 (0.016)	−0.002 (0.002)	0.0031*	0.3320
7	2.02 (0.08)	0.022 (0.012)	−0.002 (0.002)	0.0693	0.4907
8	2.91 (0.12)	0.012 (0.015)	0.003 (0.003)	0.4208	0.3807
9	2.15 (0.09)	0.035 (0.014)	0.004 (0.002)	0.0147	0.1071
10	2.31 (0.10)	0.020 (0.017)	0.002 (0.003)	0.2479	0.5526
11	2.60 (0.11)	0.067 (0.019)	0.009 (0.003)	0.0004*	0.0009*

in the size of the system matrix, which we use as a surrogate for computational effort, as discussed earlier in Sec. 4.B. The differences were strongly dependent on the pixel size and the number of measurements, whereas the magnification factor and the resolution level had much less effect on the observed differences.

In terms of RMSE, the ranking of the methods depends on the pixel size. In the MPS case, method B always yields better results than methods J and D. This observation may be attributed to the fact that method B does not simplify integration to a preferred direction, which allows avoiding artifacts around the $\pm 45^\circ$ directions. However, the advantage provided by method B was essentially marginal (<1.5 HU) in all cases. Moreover, these marginal improvements are associated with a large increase (about 50%) in computational effort (i.e., system matrix size). Also, between methods D and J, method D always yields the lowest RMSE value, but again the differences were marginal and the gain comes with a slight increase (about 5%) in computational effort. On the other hand, in the SPS case, method D appears more robust than methods B and J, but the RMSE and differences in RMSE were low in many settings, so that the RMSE advantage of method D appears to be relevant only in particular cases. In our study, these cases were G3-SPS and G7-SPS, which are the only two cases for which the reconstruction problem was underdetermined. Unfortunately, this advantage of method D comes with a major increase in computational effort (about 50%). Between methods B and J, method B yields some improvements in RMSE, but these are not sufficient for method B to compete with method D. Altogether, balancing computational effort with RMSE, we feel that method J offers the best trade-off, except in undersampled geometries where method D becomes preferable despite the increase in computational effort.

In terms of noise, basic metrics did not allow singling out a preferred method. The pixel standard deviation was clearly always larger for method J, but this effect was systematically accompanied by lower correlations between the pixels. Such differences imply that the task-based assessment of image quality is required to rank the methods. For the estimation task that we chose, we have observed that the differences in standard deviation and correlation remarkably balance out, such that all methods perform very similarly, as long as the data sampling is satisfactory to avoid major differences in RMSE. That is, in G3 and G7, method D remains preferable, whereas method J is preferred in all other settings.

6. INFLUENCE OF STATISTICAL WEIGHTS AND PENALTY TERM

An important question related to the comparative analysis presented in the previous chapters is whether such an analysis is relevant for modern iterative CT reconstruction algorithms, which typically include statistical weights as well as constraints on the image pixels. In the Introduction, we have argued that a primary goal should be to first understand what the model has to offer on its own and that reconstructions with statistical weights and a penalty term may then be

easier to understand in a second stage of investigations. To support our viewpoint, we have performed reconstruction using such features and compared the results in terms of geometrical effects. This additional study presented hereafter was restricted to two geometries, G1 and G3, both investigated using the MPS as well as the SPS setting.

Image formation for the additional study was the result of minimizing the following objective function:

$$\Psi(c) = \|W(Ac - g)\|^2 + \beta \Phi(c), \quad (14)$$

where the first term evaluates data fidelity and the second term penalizes differences between pixel values. Parameter β controls the balance between the two terms. Matrix W in the data fidelity term is a diagonal matrix that allows weighting each individual measurement. The penalty term is chosen as

$$\Phi(c) = \frac{1}{2} \sum_j \sum_{k \in \Omega_j} d_{j,k}^{-1} \phi(c_j - c_k), \quad (15)$$

where c_j and c_k represent different components of c , Ω_j identifies components c_k of c that correspond to physical neighbors of c_j , $d_{j,k}$ is the distance between the neighbors in pixel units, and $\phi(t)$ is a potential function. We only used the eight immediate neighbors. Also, the minimum of the objective function was evaluated using the iterative coordinate descent method,¹² with the iterations stopped once

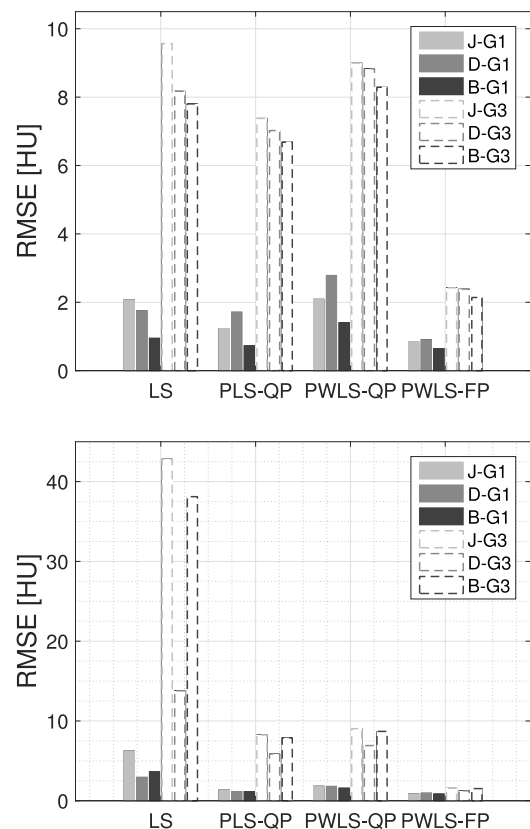


Fig. 18. RMSE at a frequency $\nu_{0.5} = 4.75/\text{cm}$ as obtained when using 3 different objective functions, referred to as PLS-QP, PWLS-QP, and PWLS-FP (see the text for details). The bars above the LS label show the result obtained with Landweber iterations; this result is supplied to facilitate comparison. (top) MPS. (bottom) SPS.

the maximum pixel update within the iteration (running sequentially over all pixels) was smaller than $10^{-4}/\text{cm}$ (i.e., about 0.5 HU).

The additional study was carried out for three different objective functions referred to as “PLS-QP,” “PWLS-QP,” and “PWLS-FP,” defined as follows:

- quadratic penalty, $\phi(t) = t^2/2$, with the same weight for all measurements, i.e., using the identity matrix for W and with β adjusted so that each model yields a resolution of $\nu_{0.5} = 4.75/\text{cm}$;
- quadratic penalty, $\phi(t) = t^2/2$, with the measurements weighted according to the fluence on the detector, i.e., using (up to a global scaling factor) the inverse square root of the variance of the data as an expression for W and with β adjusted so that each model yields a resolution of $\nu_{0.5} = 4.75/\text{cm}$;
- edge-preserving penalty, $\phi(t) = |t| - \delta \log(1 + |t/\delta|)$ with $\delta = 50$ HU, using the same weights for the measurements and the same values of β as for the second objective function.

Resolution was assessed as described in Sec. 4.A. Note that W was kept unchanged while evaluating the resolution for the second objective function. Note also that the elements of W for the second and third objective functions were scaled so that the elements of W for the central ray had a mean value of one; this scaling enabled maintaining the same resolution at high contrast for all three objective functions.

Figures 18 and 19 show the results we obtained for the RMSE, the mean standard deviation, and the mean correlation coefficient in y . The results are displayed using bar plots. Solid bars are employed for geometry G1, whereas transparent bars with dashed contour are employed for geometry G3. To facilitate comparison with the results in the previous section, we also added the bars for reconstruction using Landweber iterations; these are associated with the label “LS.” Moreover, Fig. 20 shows the Bland–Altman plots for the estimation task in the SPS case; these plots include each 1100 points (50 noise realizations, 2 geometries, and 11 locations). Other results, such as the correlation coefficients in other directions, or the Bland–Altman plots in the MPS case, are not given as they did not convey any more information.

The results in Figs. 18 and 19 show that the objective function has a global impact on the nominal values obtained for each basic metric, whereas the trends across forward projection models remain largely the same as before. For example, in the SPS case, methods J and B still yields a higher mean standard deviation and a lower correlation between pixels than method D. Also, using G3 with SPS still yields a lower RMSE with method D, although the gain is certainly not as large anymore, and the three models still yield very similar metric values in the MPS case. The following effects of the penalty term were fairly predictable: (i) RMSE is reduced in the most challenging case, namely G3-SPS, with the biggest effect observed with the edge-preserving potential and (ii) correlations between pixels are markedly increased for

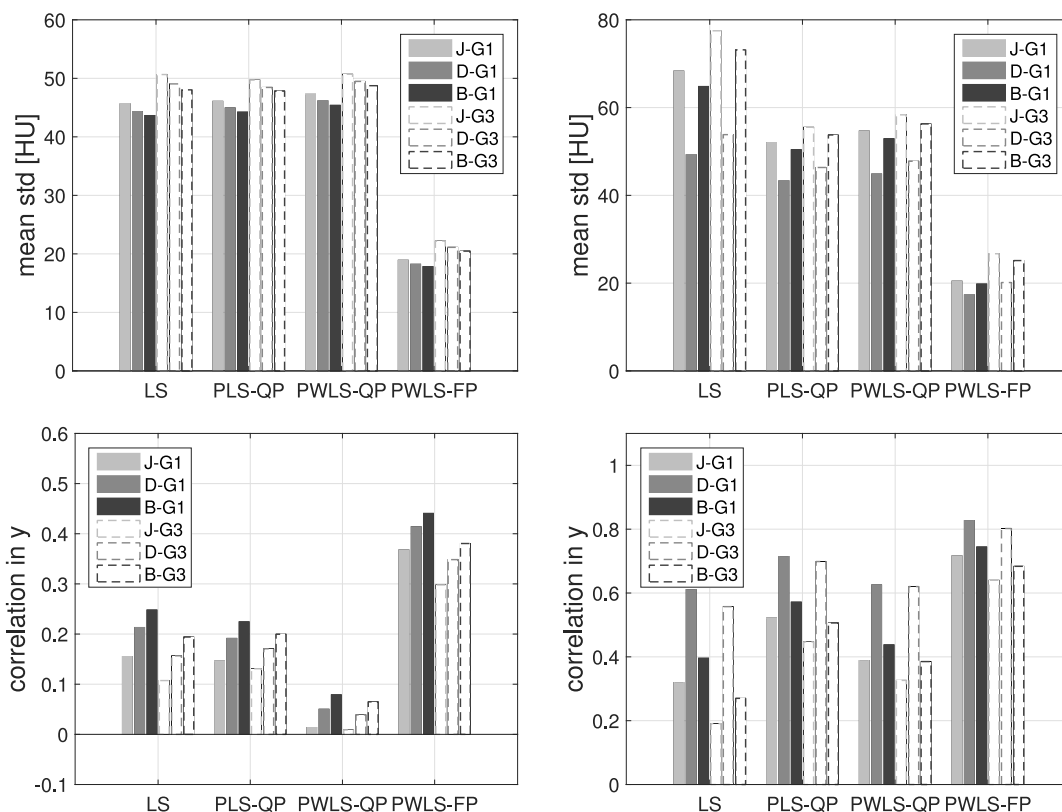


FIG. 19. Mean standard deviation (top row) and correlation in y (bottom row) when using three different objective functions, referred to as PLS-QP, PWLS-QP, and PWLS-FP (see the text for details). The bars above the LS label show the result obtained with Landweber iterations; this result is supplied to facilitate comparison. (left column) MPS. (right column) SPS.

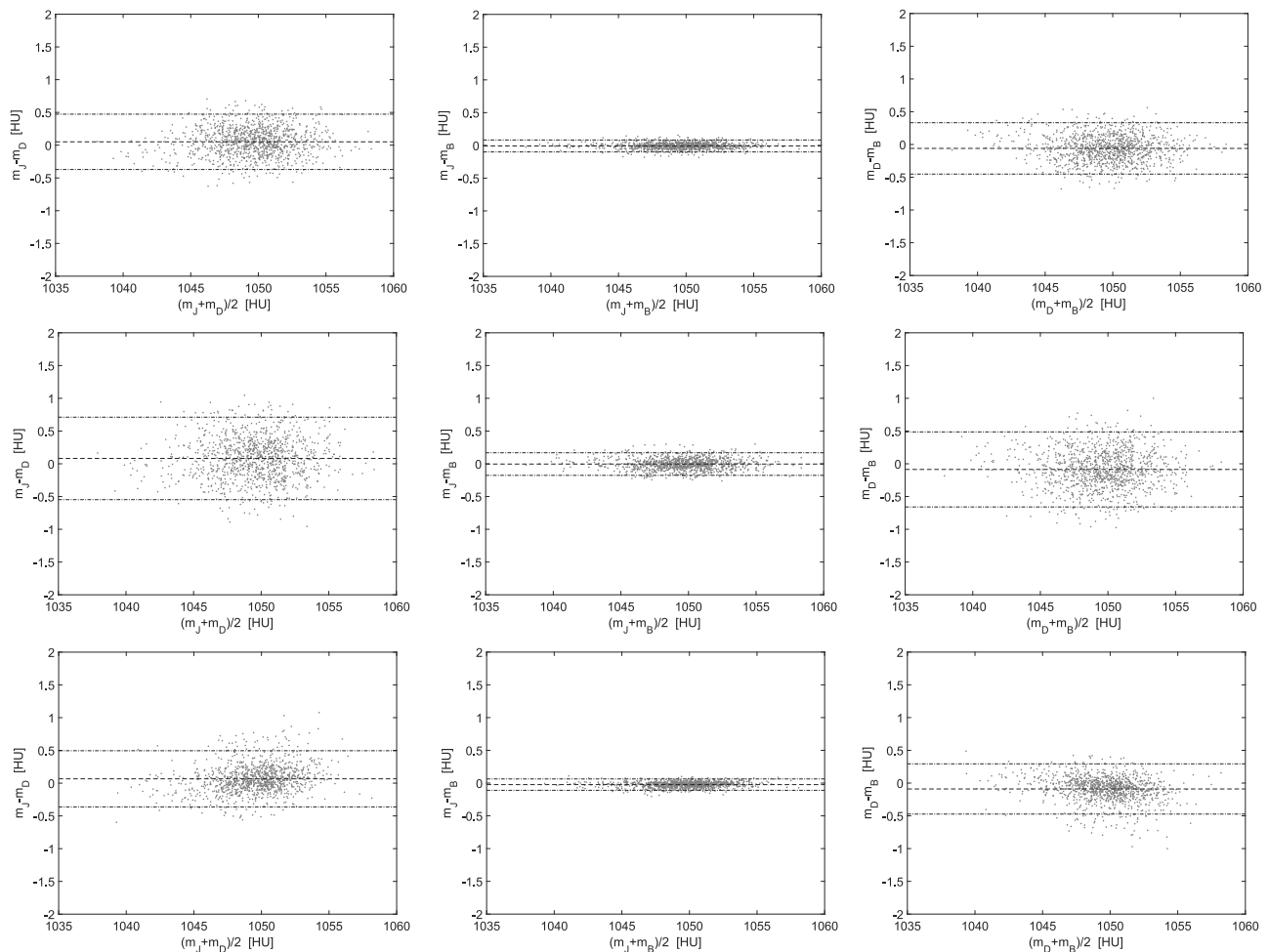


FIG. 20. Bland–Altman plots for the estimation task for the 3 different objective functions, using the SPS setting: (top row) PLS-QP; (middle row) PWLS-QP; (bottom row) PWLS-FP. Each plot includes 1100 points (2 geometries, 50 noise realization, 11 locations). Each row shows, from left to right, the plots for methods J and D, methods J and B, and methods B and D.

methods J and B in the SPS case, which previously showed low binding between the pixel values. These two effects are such that the differences between the forward projection models are strongly reduced in absolute value. Also, as expected, the statistical weights have a small negative impact on RMSE at a fixed penalty term and have a global impact on correlations. Perhaps less predictable is the change on correlations in y that is observed from one objective function to another in the MPS case, but this change is the same for all models, and thus essentially caused by the statistical weights and the penalty term altogether rather than by the forward projection model.

Likewise, the Bland–Altman plots in Fig. 20 show the same effect as before. Specifically, the differences in the mean standard deviation and correlations balance out so that all models essentially yield the same performance for all objective functions, with the added aspect that G3 can now be safely used with all models.

7. SUMMARY AND CONCLUSIONS

We presented a comparison between three forward projection models that rely on linear interpolation for iterative

reconstruction in CT. Two of these models, namely Joseph’s method and the distance-driven method, are commonly used, the first one for its simplicity and the second one for its ability to model the detector pixel size. The third method was primarily selected because it does not require the selection of a preferred Cartesian direction for the measurements, unlike the other two methods. Our comparison included a large variety of scanning geometries, and also a fair number of repeated scans in each geometry, to assess dependence on photon statistics. The geometries were the representative of contemporary CT scans. Together with the usage of two different sizes for the image pixel and a challenging phantom, they allowed a thorough investigation of the behavior of the models.

We first presented a comparison of the models on their own, using images created through Landweber iterations, which enabled observing the effect of progressively injecting components of the singular value decomposition of the projection matrix in the reconstruction. The comparison involved basic metrics covering computational effort, resolution, discretization errors (RMSE), image pixel noise, and statistical correlation between pixels and also involved an estimation task. The metrics revealed fundamental differences between the models. Two salient observations were as follows.

First, the distance-driven method is more robust than the other models when small pixels are used together with geometries with a low number of measurements. However, recall that, in such settings, the improvements provided by the distance-driven method may come with a large increase in computational effort; a change as large as 50% in the system matrix size was observed in our study. Otherwise, we feel that Joseph's method offers an attractive balance between RMSE and computational cost. When to use the distance-driven method rather than Joseph's method depends on scanned anatomy as well as reconstruction and scanning parameters and importance attributed to RMSE and computational cost.

Second, the three models yield a major difference in pixel noise as well as in correlation between pixels, so that the task-based assessment is required to rank the models. For the estimation task we selected, we observed a remarkable balancing of effects, so that all models performed similarly in geometries with sufficient measurements.

It is not straightforward to state, from our results, that all models perform similarly for detection or classification tasks in geometries with sufficient measurements. Such a statement is not even straightforward for a model observer because such tasks tend to involve the covariance matrix of the image in a nonlinear manner, whereas the estimation task involves it linearly. We have performed further comparisons of the three forward projection models using a classification task with a model observer and also using a detection task with human observers. Initial results regarding these comparisons were reported at conferences.^{83,84} These results highlight a behavior similar to that observed with the estimation task; they will be presented in detail in a future publication.

The distance-driven method might have been expected to perform better than the other models because it accounts for the finite detector size. On this aspect, note that the data simulation in this work did not only include detector blurring; it also included blurring due to the finite focal spot size and due to continuous x-ray emission. Moreover, all blurring effects were modeled using a realistic nonlinear combination of line integrals. Thus, from a physics modeling viewpoint, it is not clear that the distance-driven method is necessarily a better model.

Furthermore, we also compared the performance of the three forward projection models across geometries when forming the image using three different penalized weighted least-square objective functions. This additional study showed that the previously observed trends could still be observed, thereby providing strong support in favor of first analyzing forward projection models on their own, as performed here using Landweber iterations. Such a first analysis enables a better understanding of results obtained with complex objective functions. The additional study also showed that the penalty term can dramatically compensate for a weak RMSE, so that Joseph's method appears strongly competitive in terms of trade-off between the cost and image quality for all investigated geometries when an edge-preserving penalty is used.

The investigations we reported brought a lot of information on the behavior of important forward projection models for iterative reconstruction in diagnostic CT. However, the study was somewhat limited in that it was conducted in the 2D fan-

beam geometry. We expect that most observations would hold in 3D multislice CT, in the same way as observations related to analytical reconstruction methods generally hold from 2D to 3D. In particular, we expect the observations about pixel noise and statistical correlations between pixels to hold. In terms of bias, however, there are some uncertainties regarding windmill artifacts,⁸⁵ which could be more difficult to manage for some models than others.

ACKNOWLEDGMENTS

This work was partially supported by Siemens Medical Solutions, USA and by the U.S. National Institutes of Health (NIH) under Grant No. R01 EB007236. The concepts presented in this paper are based on research and are not commercially available. Its contents are solely the responsibility of the authors and do not necessarily represent the official views of the NIH.

CONFLICT OF INTEREST DISCLOSURE

K. Hahn, H. Schoendube, and K. Stierstorfer are employees with Siemens Healthcare GmbH. F. Noo is principal investigator on a research agreement between Siemens Medical Solutions, USA and The University of Utah.

^{a)}Electronic mail: katharina.hahn@siemens.com

^{b)}Electronic mail: noo@uair.med.utah.edu

¹A. K. Hara, R. G. Paden, A. C. Silva, J. L. Kujak, H. J. Lawder, and W. Pavlicek, "Iterative reconstruction technique for reducing body radiation dose at CT: Feasibility study," *Am. J. Roentgenol.* **193**, 764–771 (2009).

²K. T. Flicek, A. K. Hara, A. C. Silva, Q. Wu, M. B. Peter, and C. D. Johnson, "Reducing the radiation dose for CT colonography using adaptive statistical iterative reconstruction: A pilot study," *Am. J. Roentgenol.* **195**(1), 126–131 (2010).

³P. J. Pickhardt, M. G. Lubner, D. H. Kim, J. Tang, J. A. Ruma, A. M. del Rio, and G.-H. Chen, "Abdominal CT with model-based iterative reconstruction (MBIR): Initial results of a prospective trial comparing ultra low-dose with standard-dose imaging," *Am. J. Roentgenol.* **199**(6), 1266–1274 (2012).

⁴G. S. Desai, R. N. Uppot, E. W. Yu, A. R. Kambadakone, and D. V. Sahani, "Impact of iterative reconstruction on image quality and radiation dose in multidetector CT of large body size adults," *Eur. Radiol.* **22**(8), 1631–1640 (2012).

⁵V. Vardhanabhati, S. Ilyas, C. Gutteridge, S. J. Freeman, and C. A. Roobottom, "Comparison of image quality between filtered back-projection and the adaptive statistical and novel model-based iterative reconstruction techniques in abdominal CT for renal calculi," *Insights Imaging* **4**(5), 661–669 (2013).

⁶A. Neroladaki, D. Botsikas, S. Boudabbous, C. D. Becker, and X. Montet, "Computed tomography of the chest with model-based iterative reconstruction using a radiation exposure similar to chest X-ray examination: Preliminary observations," *Eur. Radiol.* **23**(2), 360–366 (2013).

⁷V. Vardhanabhati, R. D. Riordan, G. R. Mitchell, C. Hyde, and C. A. Roobottom, "Image comparative assessment using iterative reconstructions: Clinical comparison of low-dose abdominal/pelvic computed tomography between adaptive statistical, model-based iterative reconstructions and traditional filtered back projection in 65 patients," *Invest. Radiol.* **49**(4), 209–216 (2014).

⁸T. M. Buzug, *Computed Tomography: From Photon Statistics to Modern Cone-Beam CT* (Springer-Verlag, Berlin Heidelberg, 2008).

⁹C. Hofmann, M. Knaup, and M. Kachelrieß, "Effects of ray profile modeling on resolution recovery in clinical CT," *Med. Phys.* **41**(2), 021907 (14pp.) (2014).

- ¹⁰K. Zeng, B. De Man, J.-B. Thibault, Z. Yu, C. Bouman, and K. Sauer, "Spatial resolution enhancement in CT iterative reconstruction," in *2009 IEEE Nuclear Science Symposium Conference Record (NSS/MIC)* (IEEE, Piscataway, NJ, 2009), pp. 3748–3751.
- ¹¹J. Nuyts, B. De Man, J. A. Fessler, W. Zbijewski, and F. J. Beekman, "Modelling the physics in the iterative reconstruction for transmission computed tomography," *Phys. Med. Biol.* **58**(12), R63–R96 (2013).
- ¹²J.-B. Thibault, K. Sauer, C. Bouman, and J. Hsieh, "A three-dimensional statistical approach to improve image quality for multi-slice helical CT," *Med. Phys.* **34**(11), 4526–4544 (2007).
- ¹³J. A. Fessler, "Penalized weighted least-squares image reconstruction for positron emission tomography," *IEEE Trans. Med. Imaging* **13**(2), 290–300 (1994).
- ¹⁴J. Wang, T. Li, H. Lu, and Z. Liang, "Penalized weighted least-squares approach to sinogram noise reduction and image reconstruction for low-dose X-ray computed tomography," *IEEE Trans. Med. Imaging* **25**(10), 1272–1283 (2006).
- ¹⁵H. Bruder, R. Raupach, J. Sunnegårdh, M. Sedlmair, K. Stierstorfer, and T. Flohr, "Adaptive iterative reconstruction," *Proc. SPIE* **7961**, 79610J (2011).
- ¹⁶Jean-Baptiste Thibault, K. Sauer, C. Bouman, and J. Hsieh, "High quality iterative image reconstruction for multi-slice helical CT," in *International Conference on Fully 3D Reconstruction in Radiology and Nuclear Medicine, Saint Malo*, edited by Yves Bizais, Saint Malo, France, 2003, p. 4.
- ¹⁷J. Warga, "Minimizing certain convex functions," *J. Soc. Ind. Appl. Math.* **11**(3), 588–593 (1963).
- ¹⁸T. Abatzoglou and B. O'Donnell, "Minimization by coordinate descent," *J. Optim. Theory Appl.* **36**(2), 163–174 (1982).
- ¹⁹Z. Yu, J.-B. Thibault, C. A. Bouman, K. D. Sauer, and J. Hsieh, "Fast model-based X-ray CT reconstruction using spatially nonhomogeneous ICD optimization," *IEEE Trans. Image Process.* **20**(1), 161–175 (2011).
- ²⁰T. M. Benson, B. De Mann, L. Fu, and J. B. Thibault, "Block-based iterative coordinate descent," in *2010 IEEE Nuclear Science Symposium, Medical Imaging Conference* (IEEE, New York, 2010), pp. 2856–2859.
- ²¹J. A. Fessler and D. Kim, "Axial block coordinate descent (ABCD) algorithm for X-ray CT image reconstruction," in *Proceedings of the 11th International Meeting on Fully 3D Image Reconstruction in Radiology and Nuclear Medicine*, edited by Marc Kachelriess, Potsdam, Germany, 2011, pp. 262–265.
- ²²Y. Nesterov, A method of solving a convex programming problem with convergence rate $O(1/k^2)$. In *Soviet Mathematics Doklady*, volume 27, pages 372–376, 1983.
- ²³Y. Nesterov, "Smooth minimization of non-smooth functions," *Math. Program.* **103**(1), 127–152 (2005).
- ²⁴Y. Nesterov, "Gradient methods for minimizing composite objective function," in *CORE Discussion Paper 2007/76* (2007).
- ²⁵A. Beck and M. Teboulle, "A fast iterative shrinkage-thresholding algorithm for linear inverse problems," *SIAM J. Imaging Sci.* **2**(1), 183–202 (2009).
- ²⁶J. Sunnegårdh, "Iterative filtered backprojection methods for helical cone-beam CT," Ph.D. thesis, Linköping University Electronic Press, 2009.
- ²⁷H. Hudson and R. Larkin, "Accelerated image reconstruction using ordered subsets of projection data," *IEEE Trans. Med. Imaging* **13**(4), 601–609 (1994).
- ²⁸C. Kamphuis and F. J. Beekman, "Accelerated iterative transmission CT reconstruction using an ordered subsets convex algorithm," *IEEE Trans. Med. Imaging* **17**(6), 1001–1105 (1998).
- ²⁹H. Erdogan and J. A. Fessler, "Ordered subsets algorithm for transmission tomography," *Phys. Med. Biol.* **44**(11), 2835–2851 (1999).
- ³⁰Dimitri P Bertsekas, "Incremental proximal methods for large scale convex optimization," *Math. Program.* **129**(2), 163–195 (2011).
- ³¹D. Kim *et al.*, "Accelerating ordered subsets image reconstruction for X-ray CT using spatially nonuniform optimization transfer," *IEEE Trans. Med. Imaging* **32**(11), 1965–1978 (2013).
- ³²H. Nien *et al.*, "Fast X-ray CT image reconstruction using a linearized augmented Lagrangian method with ordered subsets," *IEEE Trans. Med. Imaging* **34**(2), 388–399 (2015).
- ³³D. Kim *et al.*, "Combining ordered subsets and momentum for accelerated X-ray CT image reconstruction," *IEEE Trans. Med. Imaging* **34**(1), 167–178 (2015).
- ³⁴J. Zheng *et al.*, "Parallelizable Bayesian tomography algorithms with rapid, guaranteed convergence," *IEEE Trans. Med. Imaging* **9**(10), 1745–1759 (2000).
- ³⁵K. Mueller and R. Yagel, "Rapid 3-D cone-beam reconstruction with the simultaneous algebraic reconstruction technique (SART) using 2-D texture mapping hardware," *IEEE Trans. Med. Imaging* **19**(12), 1227–1237 (2000).
- ³⁶F. Xu and K. Mueller, "Accelerating popular tomographic reconstruction algorithms on commodity PC graphics hardware," *IEEE Trans. Nucl. Sci.* **52**(3), 654–663 (2005).
- ³⁷F. Xu and K. Mueller, "Real-time 3D computed tomographic reconstruction using commodity graphics hardware," *Phys. Med. Biol.* **52**(12), 3405–3419 (2007).
- ³⁸M. Kachelriess, M. Knaup, and O. Bockenbach, "Hyperfast parallel-beam and cone-beam backprojection using the cell general purpose hardware," *Med. Phys.* **34**(4), 1474–1486 (2007).
- ³⁹S. Steckmann, M. Knaup, and M. Kachelriess, "High performance cone-beam spiral backprojection with voxel-specific weighting," *Phys. Med. Biol.* **54**(12), 3691–3708 (2009).
- ⁴⁰J. K. Kim *et al.*, "Forward-projection architecture for fast iterative image reconstruction in X-ray CT," *IEEE Trans. Signal Process.* **60**(10), 5508–5518 (2012).
- ⁴¹E. Papenhausen, Z. Zheng, and K. Mueller, "Creating optimal code for GPU-accelerated CT reconstruction using ant colony optimization," *Medical physics* **40**(3), 031110 (7pp.) (2013).
- ⁴²C. G. Graff and E. Y. Sidky, "Compressive sensing in medical imaging," *Appl. Opt.* **54**(8), C23–C44 (2015).
- ⁴³G.-H. Chen, J. Tang, and S. Leng, "Prior image constrained compressed sensing (PICCS): A method to accurately reconstruct dynamic CT images from highly undersampled projection data sets," *Med. Phys.* **35**(2), 660–663 (2008).
- ⁴⁴J. Yang, H. Yu, M. Jiang, and G. Wang, "High-order total variation minimization for interior tomography," *Inverse Probl.* **26**(3), 035013 (2010).
- ⁴⁵G. Wang and H. Yu, "The meaning of interior tomography," *Phys. Med. Biol.* **58**(16), R161–R186 (2013).
- ⁴⁶P. Sukovic and Neal H. Clinthorne, "Penalized weighted least-squares image reconstruction for dual energy X-ray transmission tomography," *IEEE Trans. Med. Imaging* **19**(11), 1075–1081 (2000).
- ⁴⁷H. Gao, H. Yu, S. Osher, and G. Wang, "Multi-energy CT based on a prior rank, intensity and sparsity model (PRISM)," *Inverse Probl.* **27**(11), 115012 (2011).
- ⁴⁸C. O. Schirra *et al.*, "Statistical reconstruction of material decomposed data in spectral CT," *IEEE Trans. Med. Imaging* **32**(7), 1249–1257 (2013).
- ⁴⁹R. Zhang *et al.*, "Model-based iterative reconstruction for dual-energy X-ray CT using a joint quadratic likelihood model," *IEEE Trans. Med. Imaging* **33**(1), 117–134 (2014).
- ⁵⁰Y. Long *et al.*, "Multi-material decomposition using statistical image reconstruction for spectral CT," *IEEE Trans. Med. Imaging* **33**(8), 1614–1626 (2014).
- ⁵¹A. Sawatzky *et al.*, "Proximal ADMM for multi-channel image reconstruction in spectral X-ray CT," *IEEE Trans. Med. Imaging* **33**(8), 1657–1668 (2014).
- ⁵²Q. Xu, A. Sawatzky, M. A. Anastasio, and C. O. Schirra, "Sparsity-regularized image reconstruction of decomposed K-edge data in spectral CT," *Phys. Med. Biol.* **59**(10), N65–N79 (2014).
- ⁵³P. M. Joseph, "An improved algorithm for reprojecting rays through pixel images," *IEEE Trans. Med. Imaging* **1**(2), 192–196 (1982).
- ⁵⁴R. L. Siddon, "Fast calculation of the exact radiological path for a three-dimensional CT array," *Med. Phys.* **12**(2), 252–255 (1985).
- ⁵⁵S.-C. B. Lo, "Strip and line path integrals with a square pixel matrix: A unified theory for computational CT projections," *IEEE Trans. Med. Imaging* **7**(4), 355–363 (1988).
- ⁵⁶R. M. Lewitt, "Multidimensional digital image representations using generalized Kaiser-Bessel window functions," *J. Opt. Soc. Am. A* **7**(10), 1834–1846 (1990).
- ⁵⁷F. Jacobs, E. Sundermann, B. De Sutter, M. Christiaens, and I. Lemahieu, "A fast algorithm to calculate the exact radiological path through a pixel or voxel space," *J. Comput. Inf. Technol.* **6**(1), 89–94 (1998).
- ⁵⁸H. Turbell, "Cone-beam reconstruction using filtered backprojection," Ph.D. thesis, Linköping University Electronic Press, 2001.
- ⁵⁹S. Horbelt, M. Liebling, and M. Unser, "Discretization of the Radon transform and of its inverse by spline convolutions," *IEEE Trans. Med. Imaging* **21**(4), 363–376 (2002).
- ⁶⁰B. De Man and S. Basu, "Distance-driven projection and backprojection," in *2002 IEEE Nuclear Science Symposium Conference Record* (IEEE, Norfolk, 2002), Vol. 3, pp. 1477–1480.

- ⁶¹J. F. Williamson, B. R. Whiting, J. Benac, R. J. Murphy, G. James Blaine, J. A. OSullivan, D. G. Politte, and D. L. Snyder, "Prospects for quantitative computed tomography imaging in the presence of foreign metal bodies using statistical image reconstruction," *Med. Phys.* **29**(10), 2404–2418 (2002).
- ⁶²A. Ziegler, T. Köhler, T. Nielsen, and R. Proksa, "Efficient projection and backprojection scheme for spherically symmetric basis functions in divergent beam geometry," *Med. Phys.* **33**(12), 4653–4663 (2006).
- ⁶³B. Zhang and G. L. Zeng, "An immediate after-backprojection filtering method with blob-shaped window functions for voxel-based iterative reconstruction," *Phys. Med. Biol.* **51**(22), 5825–5842 (2006).
- ⁶⁴Y. Long *et al.*, "3D forward and back-projection for X-ray CT using separable footprints," *IEEE Trans. Med. Imaging* **29**(11), 1839–1850 (2010).
- ⁶⁵F. Noo, K. Schmitt, K. Stierstorfer, and H. Schondube, "Image representation using mollified pixels for iterative reconstruction in X-ray CT," in *2012 IEEE Nuclear Science Symposium and Medical Imaging Conference (NSS/MIC)* (IEEE, Anaheim, CA, 2012), pp. 3453–3455.
- ⁶⁶A. C. Kak and M. Slaney, *Principles of Computerized Tomographic Imaging* (Society for Industrial and Applied Mathematics, Philadelphia, PA, 2001).
- ⁶⁷W. Zbijewski and F. J. Beekman, "Characterization and suppression of edge and aliasing artefacts in iterative x-ray CT reconstruction," *Phys. Med. Biol.* **49**(1), 145–157 (2003).
- ⁶⁸B. De Man and S. Basu, "Distance-driven projection and backprojection in three dimensions," *Phys. Med. Biol.* **49**, 2463–2474 (2004).
- ⁶⁹L. Fu, J. Wang, X. Rui, Jean-Baptiste Thibault, and B. De Man, "Modeling and estimation of detector response and focal spot profile for high-resolution iterative CT reconstruction," in *2013 IEEE Nuclear Science Symposium and Medical Imaging Conference (NSS/MIC)* (IEEE, Seoul, Korea, 2013), pp. 1–5.
- ⁷⁰Q. Xu, E. Y. Sidky, X. Pan, M. Stampanoni, P. Modregger, and M. A. Anastasio, "Investigation of discrete imaging models and iterative image reconstruction in differential X-ray phase-contrast tomography," *Opt. Express* **20**(10), 10724–10749 (2012).
- ⁷¹G. H. Golub and C. F. van Loan, *Matrix Computations* (John Hopkins University, Baltimore, MD, 1996).
- ⁷²Z. Rumboldt, W. Huda, and J. W. All, "Review of portable CT with assessment of a dedicated head CT scanner," *Am. J. Neuroradiology* **30**(9), 1630–1636 (2009).
- ⁷³<http://www.imp.uni-erlangen.de/phantoms>.
- ⁷⁴Z. Yu, F. Noo, F. Dennerlein, A. Wunderlich, G. Lauritsch, and J. Hornegger, "Simulation tools for two-dimensional experiments in X-ray computed tomography using the FORBILD head phantom," *Phys. Med. Biol.* **57**, N237–N252 (2012).
- ⁷⁵A. Wunderlich and F. Noo, "Image covariance and lesion detectability in direct fan-beam X-ray computed tomography," *Phys. Med. Biol.* **53**, 2471–2493 (2008).
- ⁷⁶T. G. Flohr, K. Stierstorfer, S. Ulzheimer, H. Bruder, A. N. Primak, and C. H. McCollough, "Image reconstruction and image quality evaluation for a 64-slice CT scanner with z-flying focal spot," *Med. Phys.* **32**(8), 2536–2547 (2005).
- ⁷⁷H. H. Barrett and K. J. Myers, *Foundations of Image Science* (Wiley, Hoboken, NJ, 2004).
- ⁷⁸J. Martin Bland and D. Altman, "Statistical methods for assessing agreement between two methods of clinical measurement," *Lancet* **327**(8476), 307–310 (1986).
- ⁷⁹R. J. Muirhead, *Aspects of Multivariate Statistical Theory* (John Wiley & Sons, New York, 2009), Vol. 197.
- ⁸⁰A. K. Gupta and D. K. Nagar, *Matrix Variate Distributions* (CRC, London, 1999), Vol. 104.
- ⁸¹T. W. Anderson, *The statistical Analysis of Time Series* (John Wiley & Sons, New York, 2011), Vol. 19.
- ⁸²G. Casella and R. L. Berger, *Statistical Inference* (Duxbury Pacific Grove, CA, 2002), Vol. 2.
- ⁸³K. Schmitt, H. Schondube, K. Stierstorfer, J. Hornegger, and F. Noo, "Task-based comparison of linear forward projection models in iterative CT reconstruction," in *Proceedings of the Third International Conference on Image Formation in X-ray Computed Tomography*, edited by Frédéric Noo (Salt Lake City, UT, 2014), pp. 56–59.
- ⁸⁴K. Hahn, U. Rassner, H. C. Davidson, H. Schöndube, K. Stierstorfer, J. Hornegger, and F. Noo, "Iterative CT reconstruction with small pixel size: Distance-driven forward projector versus Joseph's," *Proc. SPIE* **9412**, 94123D (2015).
- ⁸⁵M. D. Silver, K. Taguchi, I. A. Hein, B. Chiang, M. Kazama, and I. Mori, "Windmill artifact in multislice helical CT," *Proc. SPIE* **5032**, 1918–1927 (2003).